REPORT DOCUMENTATION PAGE

Form Approved
OMB No. 0704-01-0188

1. REPORT DATE *(DD-MM-YYYY)*	2. REPORT TYPE	3. DATES COVERED *(From - To)*
20–10–2004	Final Report	

4. TITLE AND SUBTITLE	5a. CONTRACT NUMBER
	N66001-01-1-8036

PHOTONIC INTEGRATED TRANSMITTER AND RECEIVER COMPONENTS FOR RF LINKS WITH GAIN FINAL REPORT

5b. GRANT NUMBER

5c. PROGRAM ELEMENT NUMBER

6. AUTHORS

L. Coldren, D.Cohen,, J. Piprek, D. Lasaosa, Y-J. Ciu, D. Pasquariello, H-F Chou, K-G Gan, H. Shi, J-W Shi, E. Skogen, J. Barton, J. Dolen, M. Majewski, J. Getty, J. Nolde, L. Johansson, B. Liu, J. Shim, A. Keating: UCSB

Y. Akulova: Agility Communications

5d. PROJECT NUMBER

5e. TASK NUMBER

5f. WORK UNIT NUMBER

7. PERFORMING ORGANIZATION NAME(S) AND ADDRESS(ES)

University of California
Electrical and Computer
  Engineering Department
Santa Barbara, CA 93106

Agility Communications
475 Pine Avenue
Santa Barbara, CA 93117

SSC San Diego
Program Monitor: J. Hodiak
San Diego, CA 92152-5001

8. PERFORMING ORGANIZATION REPORT NUMBER

9. SPONSORING/MONITORING AGENCY NAME(S) AND ADDRESS(ES)

Defense Adavanced Research Projects Agency
Microsystems Technology Office
Arlington, VA 22203-1714

10. SPONSOR/MONITOR'S ACRONYM(S)
DARPA\MTO

11. SPONSOR/MONITOR'S REPORT NUMBER(S)

12. DISTRIBUTION/AVAILABILITY STATEMENT

Approved for public release; distribution is unlimited.

13. SUPPLEMENTARY NOTES

14. ABSTRACT

Optical links have many advantages over microwave links for a wide range of applications, including phased array radars, antennas, remoting, and microwave signal processing. Some major limitations in the deployment of optical links has been the large drive voltages, link loss, and limited linearity. The goal of the UCSB program was the demonstration of novel device concepts, innovative integration techniques, and interesting link concepts to address these issues. Significant contributions have been made in all these areas, including very low voltage traveling wave modulators with a V_π of 0.35 V, exceeding the program goal of 0.5 V, electroabsorption modulators integrated with tunable lasers, and novel links to simultaneously reduce the second and third order nonlinearity. The report provides details on devices, circuits, links, and their performance.

15. SUBJECT TERMS
Mission Area: Command and Control
| optical links | electroabsorption | tunable optical transmitter chip | modulation |
| traveling wave | nonlinearity | amplification photodector | |

16. SECURITY CLASSIFICATION OF:

a. REPORT	b. ABSTRACT	c. THIS PAGE	17. LIMITATION OF ABSTRACT	18. NUMBER OF PAGES	19a. NAME OF RESPONSIBLE PERSON
U	U	U	UU	13	C. Hanson

19B. TELEPHONE NUMBER *(Include area code)*
(619) 553-5242/2164

Standard Form 298 (Rev. 8/98)
Prescribed by ANSI Std. Z39.18

February 2005

Photonic Integration Transmitter and Receiver Components for RF Links with Gain Final Report

L. Coldren, D.Cohen,, J. Piprek, D. Lasaosa,
Y-J Ciu, D. Pasquariello, H-F Chou,
K-G Gan, H. Shi, J-W Shi, E. Skogen,
J. Barton, J. Dolen, M. Majewski, J. Getty,
J. Nolde, L. Johansson, B. Liu, J. Shim, A. Keating
UCSB

Y. Akulova
Agility Communications

SSC San Diego

Photonic Integrated Transmitter and Receiver Components for RF Links with Gain

Optical links have many advantages over microwave links for a wide range of applications, including phased array radars, antenna remoting, microwave signal processing. Some of the major limitations in the deployment of optical links has been the large drive voltages, link loss, and limited linearity. The goal of the UCSB program was the demonstration of novel device concepts, innovative integration techniques and interesting link concepts to address these issues. We have made significant contributions in all of these areas, including very low voltage traveling wave modulators with a V_π of 0.35 V, exceeding the program goal of 0.5 V, EAMs integrated with tunable lasers, and novel links to simultaneously reduce the second and third order nonlinearity. The remainder of this section gives a summary of these results, and the rest of this report gives details on the devices, circuits, links and their performance.

Summary of Results

Traveling-wave electroabsorption modulators
High performance traveling-wave electroabsorption modulators (EAMs) were developed at UCSB. The EAMs were optimized for analog applications, with large dynamic range, good linearity, high speed, and low drive voltage being important parameters. The combination of the quantum confined Stark effect (QCSE) with a traveling wave electroabsorption modulator (TWEAM) resulted in record low drive voltages. The performance of the EAMs in an analog link was investigated. The results are, in summary:

- 3-dB bandwidth of 40 GHz.
- A high slope efficiency of > 4/V at 1.55μm for a 300 μm long EAM was measured, which is equivalent to a Mach-Zehnder modulator with a V_π of 0.37 V.
- A spurious-free dynamic range (SFDR) as high as 128dB-Hz$^{4/5}$ at 10 GHz has been achieved experimentally.
- With the help of an EDFA, a link gain of 1 dB at 10 GHz has been successfully demonstrated.
- A novel demonstration of simultaneous reduction of 2nd and 3d order nonlinearities through the use of two wavelengths through the modulator

Tunable optical transmitter chips
Agility Communications developed integrated optical transmitter chips comprised of a Sampled-Grating Distributed Bragg Reflector (SG-DBR) laser monolithically integrated with a Semiconductor Optical Amplifier (SOA) and a high-speed Electroabsorption (EA) or Mach-Zehnder (MZ) modulator. Prototypes of developed components (chip-on-carriers (CoCs), laser diode modules (LDMs), and LDMs integrated with control boards) were provided for RF experiments. Performance of the integrated devices over a 40 nm wavelength tuning range include:

3

20061130029

SGDBR-SOA
- High output power (>80 mW)
- SMSR > 40 dB
- Linewidth < 5 MHz

SGDBR-SOA-EAM chips
- High output power (>30 mW over 40 nm range)
- Excellent EAM power handling (> 300 mW electrical)
- 3dB BW > 6.5 GHz
- Under digital modulation devices meet the requirements of OC-48 with FEC
- 350 km reach at 2.5 Gb/s in standard SMF

SGDBR-SOA-MZM chips:
- 3dB BW > 10 GHz
- Output power of >20 mW over 40 nm rangeConfigurable chirp
- Under digital modulation devices meet the requirements of OC-192
- 100 km reach at 10 Gb/s in standard SMF

Analog characterization of transmitter chip
The integrated optical transmitters were characterized for analog applications, the results are summarized below.

SGDBR direct modulation performance:
- 112dB/Hz$^{2/3}$ SFDR.
- Up to 8 GHz bandwidth
- Gain-levered SGDBR lasers produced for enhanced modulation efficiency.

Bipolar Cascade Series-connected Lasers:
- Up to 390% DQE achieved for a 12-stage F-P laser
- 50-Ohm matching achieved for a 3-stage F-P laser
- 112dB/Hz$^{2/3}$ SFDR achieved for a 3-stage F-P laser
- Bipolar cascade series-connected SGDBR lasers produced

SGDBR-SOA-EAM analog performance:
- <154 dB/Hz RIN
- SFDR in the 125-127 dB/Hz$^{4/5}$–range over the tuning range
- 32dB NF and -21dB Gain achieved

SGDBR-SOA-MZM analog performance:
- 3dB BW > 40 GHz for 35-Ohm terminated device
- 106.6 dB·Hz$^{2/3}$ to 111.2 dB·Hz$^{2/3}$ SFDR over tuning range.

Traveling wave amplification photodetectors
Novel traveling wave amplification photodetectors (TAP detectors) were developed at UCSB. GaAs-based devices were designed and fabricated for operation at 850-nm wavelength and InP based devices were demonstrated for 1550 nm operation. A detailed traveling wave noise theory was developed. Three TAP structures were investigated

4

(sequential longitudinal, laterally coupled and vertically coupled). Over 200% quantum efficiency was achieved with these devices.

Irradiation Studies
QCSE TWEAMs from UCSB and SGDBR-SOA-modulator chips from Agility were sent to Innovative Concepts, Inc. for proton irradiation studies. The results of the irradiation experiments indicated that the chips are sufficiently robust with large margins, in all but the most extreme orbital conditions and under very little shielding, to withstand space radiation environments likely to be encountered by government and commercial applications.

1. Electroabsorption Modulators

The development of high-performance electroabsorption modulators (EAMs) have been a central part of this 4-year project. One important goal was the integration of high-speed EAMs with widely tunable DBR lasers as described in Section 2 of this report. The development and analysis of discrete traveling-wave EAMs with high modulation bandwidth, low drive voltage, and large dynamic range is described in the present section.

1.1 Introduction

Electroabsorbtion modulators (EAMs) are ideal external modulators in RF links. Their advantages include high modulation bandwidth, low drive voltage, high efficiency, high extinction ratio, low chirp, and large spur-free dynamic range (SFDR). The technology also lends itself to integration with other optoelectronic devices in photonic integrated circuits (PICs). EAMs function through the change in material absorption in the presence of an electric field. This function is either based on the Franz-Keldysh effect for the case of bulk active regions, or the quantum confined stark effect (QCSE) for quantum well (QW) EAMs. In QW material, there exist an absorption peak below the bandgap energy, stemming from exciton resonances (Coulomb interaction between electrons and holes). The excitons are confined by the QWs and hence does not get separated by the applied electric field as they would in bulk material. Compared to the Franz-Keldysh effect, the absorption edge of QWs is much sharper and moves faster with changes in a reverse biased electric field.
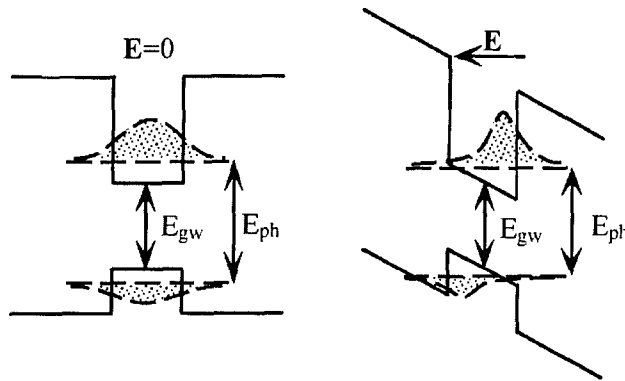

Figure 1.1. Quantum confined Stark effect.

EAMs can be made as either lumped elements or traveling-wave devices. Figure 1.2 shows a comparison of the device structure of lumped and traveling-wave EAMs. In the lumped electron configuration, the microwave signal is applied in the center of the optical waveguide, and will therefore experience strong reflection at the ends of the waveguide. As a result of this, the intrinsic speed of the device is limited by the RC time constant. In practice, a 50-Ω load is usually used to reduce microwave reflection back to the driver. In order to maximize the speed of the device, the capacitance has to be minimized, meaning the device length should be minimized. The short length will increase the drive voltage, decrease the saturation power, and make the device difficult to handle and package. Using the traveling-wave configuration, the microwave is applied to the end of the optical waveguide and copropagates with the optical signal. At the output

6

end the microwave signal is terminated by a matching load in order to minimize back reflections. The RC limitations of the lumped device are overcome, resulting in higher speed and lower drive voltage. Because the modulation bandwidth is independent of device length, longer devices can be tolerated, which result in higher saturation power without compromising extinction ratio.
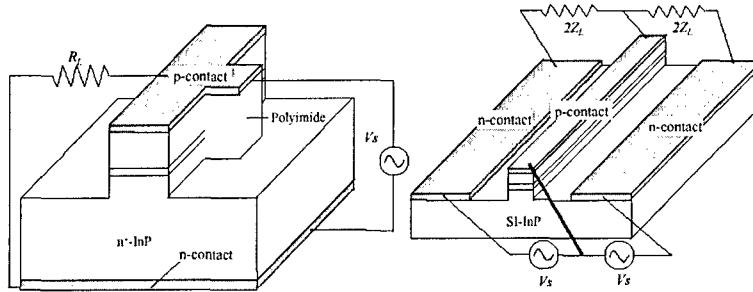

Figure 1.2. Comparison of lumped and traveling-wave modulators.

1.2 First Generation EAMs

All EAMs designed in this project were designed to be traveling-wave structures. The epilayer material was InGaAsP-based, grown by MOCVD on a semi-insulating InP substrate. In the first generation of devices, the active region consisted of 10 strained QWs (-0.31% tensile strain) and 11 strain compensating barriers (0.57% compressive strain). The width of the QWs and barriers were 10.4 nm and 7.6 nm, respectively. The active region was sandwiched between cladding layers of 1.7 μm p-InP (top) and 0.4 μm n-InP (bottom). 300-μm long ridge-waveguide type EAMs were fabricated. The ridge was formed by $CH_3/H_2/Ar$ reactive ion etching (RIE). PMGI was utilized for passivating the etching surface, the planarization, and the bridge of the CPW lines interconnection. Two CPW lines forming the traveling-wave circuit were used for the microwave power feed line and output impedance matching. The EAM was terminated by 50 Ω in order to reduce electrical reflections. Figure 1.3 shows the top view of the device (left). A scanning electron micrograph (SEM) of the cross-section of the device is shown in to the right in Figure 1.3.
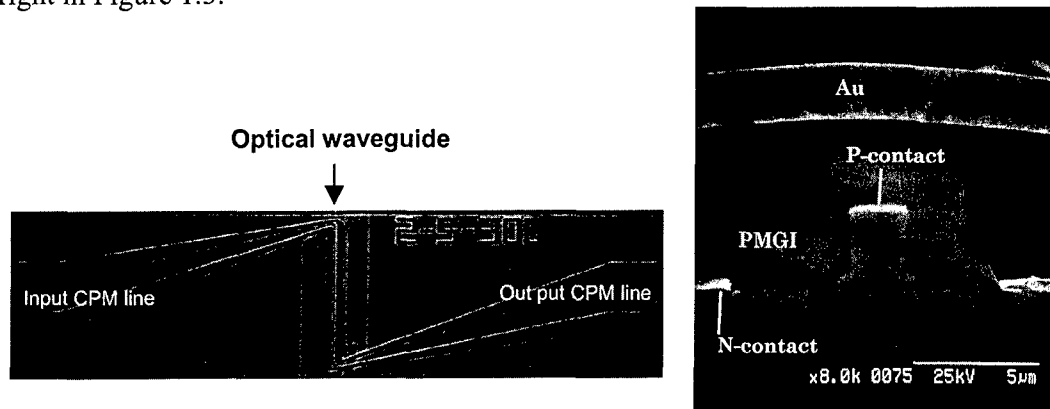

Figure 1.3. Images of fabricated EAM. Top view (left) and cross-section (right).

7

Figure 1.4 shows the fiber-to-fiber transmission vs. reverse bias for 1555-nm wavelength. A 20-dB extinction ratio was achieved for only 1 V reverse bias, for both the TE and the TM modes. Transmission vs. optical input power is shown in Figure 1.5. No power saturation was observed up to 10 dBm optical input power. Figure 1.6 shows the optically pre-amplified eye diagram at 10 Gb/s for a bit error rate (BER) of 10^{-9}. BER vs. received power for a 2^{31}-1 pseudorandom bit sequence (PRBS) is shown in Figure 1.7. The optical input power was 9 dBm. Error-free operation was achieved with a receiver sensitivity of –32.5dBm. The applied reverse bias was below 0.7 V and the driving voltage was 1 V_{p-p} for both polarization states.
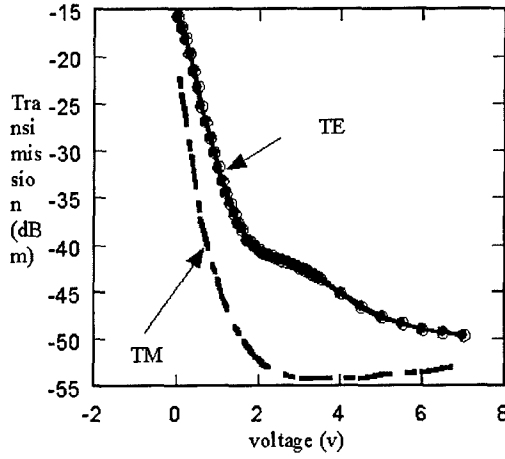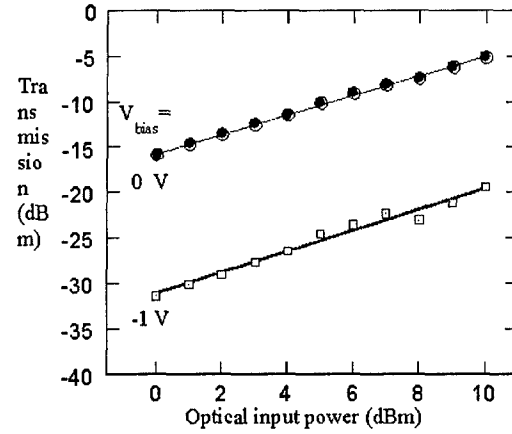

Figure 1.4. Transmission vs. reverse bias.

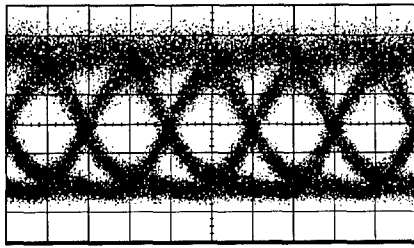Figure 1.5. Transmission vs. optical power.
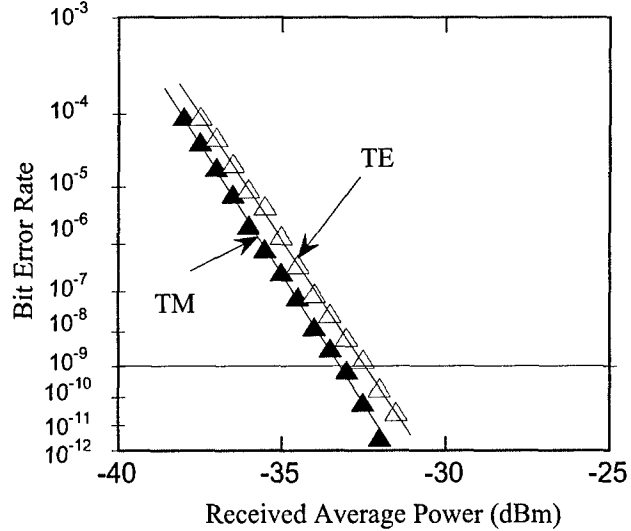

Figure 1.6. 10 Gb/s eye diagram.

Figure 1.7. BER versus received power.

1.3 Modeling and Optimization

In order to optimize out EAM structure for linearity, high speed, and high efficiency, we developed a time-dependent distributed elements model that includes the distributed absorption and chirping effects between optical wave and microwave. To model the microwave characteristics accurately, the feed lines and termination need to be included.

For this purpose, an equivalent circuit model was developed and the microwave propagation calculation was based on a linear two-port frequency domain transmission matrix method.

Figures 1.8 and 1.9 show the simulated and measured S21 (left) and S11 (right) for different lengths of devices. Calculated results are quite consistent with the measured results, verifying the two-port equivalent circuit model. Small microwave field attenuations (0.2 dB/100μm at 20 GHz, 0.5 dB/100μm at 50 GHz) were obtained from the straight waveguide. However, the total port-to-port S21 transmission of the device is about −3 dB and −5 dB loss at 20 GHz and 50 GHz respectively. Except the higher microwave loss due to the long device, it also indicates that the high impedance mismatching between the feed lines and waveguides causes about -1.4 dB and −3.5 dB penalty at 20 GHz and 50 GHz. Furthermore, the S11 shows that the reflection goes up to −5 dB as frequency up to 20 GHz, which is mainly due to the high impedance mismatch. There are clear reflection reductions at the higher frequency. For longer devices, a reflection dip occurs at lower frequency, suggesting that the Fabry-Perot effects build up due to the long feed lines.
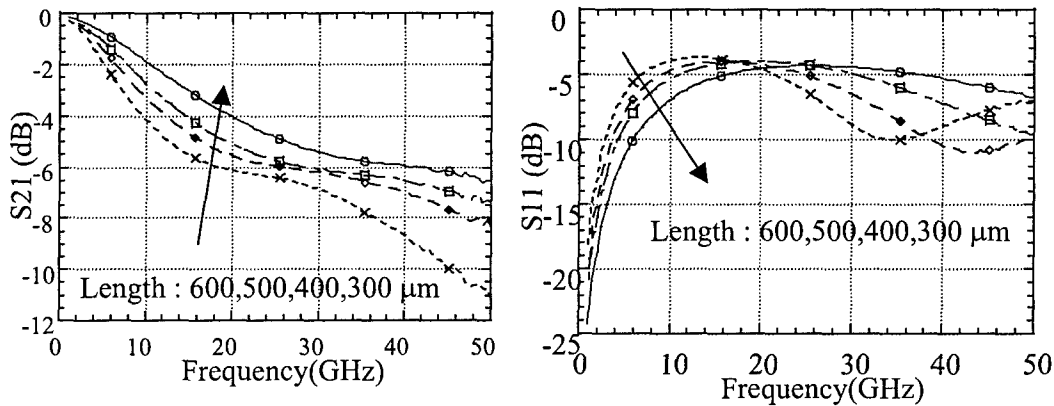

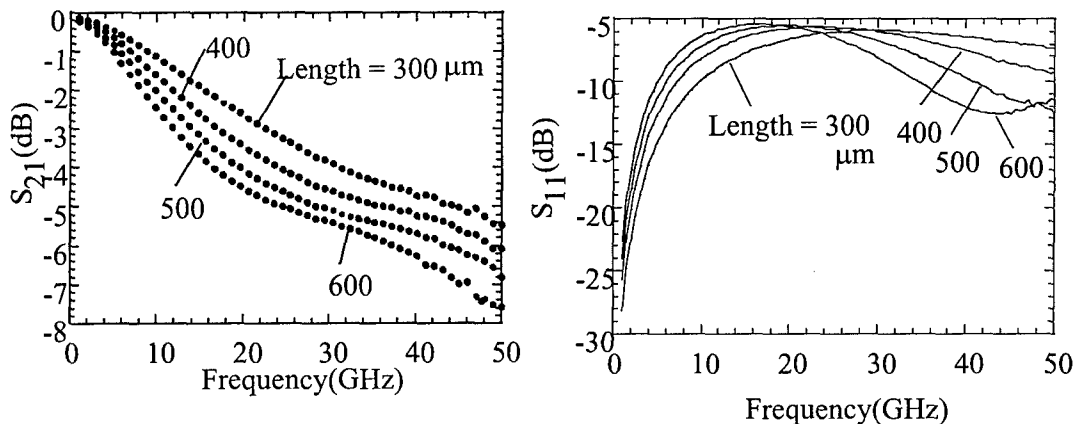Figure 1.8. Simulated S21 and S11 for different length EAMs (600μm to 300μm).

Figure 1.9. Measured S21 and S11 for different length EAMs.

9

1.4 Second Generation EAMs

The objectives of the second generation EAMs were to improve modulation efficiency and saturation power. Wider wells and lower barriers were used compared to Generation 1. Bandgap engineering was performed to avoid decreasing the extinction ratio due to the reduced bandgap offset. The active region consisted of 10 strained QWs (-0.35% tensile strain) and 11 strain compensating barriers (0.57% compressive strain). The width of the QWs were 12 nm, compared to 10.4 nm in Generation 1. The barrier width was increased to 7.6 nm from 7 nm. Except for the QW design, the structure was similar to Generation 1. There were no major changes in the fabrication.

Figure 1.10 shows the normalized lens-coupled fiber-to-fiber transmission measurement (TM-mode) as function of bias for an optical power of 2 dBm at a wavelength of 1555 nm. The insertion loss at D.C is about 12 dB for a forward bias of 1 V. The total coupling loss for both facets is about 5 to 6 dB. As shown in Figure 1.10, a total extinction ratio of 57 dB (from 1 V forward bias to 4.5 V reverse bias) is achieved. It should be noted that the modulation efficiency is higher than 30 dB/V for 0 V to 1 V, while the modulation depth is 40 dB for the bias from 0 V to 2 V. High extinction ratio driven by lower swing voltage is mainly attributed to the improved active region.
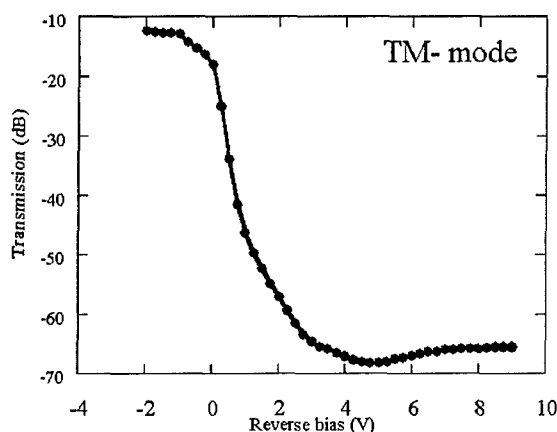

Figure 1.10. Fiber-to-fiber transmission vs. reverse bias.

The frequency response was measured by a HP Lightwave Component Network analyzer (HP8703A). The device was terminated by a 35-Ω chip resistance with ribbon bonding for obtaining broadband response. As shown in Figure 1.11, a flat response was obtained with 1.5 dB drop at 20 GHz. The device is biased at V = 0.4 V. A distributed model (solid curve in Figure 1.11) was used to fit the experimental results, where the expected 3-dB bandwidth is about 40 GHz. The microwave characteristics used in this model for this calculation are extracted from the S-parameters measurements on the straight waveguides. The improved microwave attenuation (0.2 dB/100μm at 20 GHz) and flatter frequency response is mainly attributed to decreasing the parasitic capacitance on the waveguide.
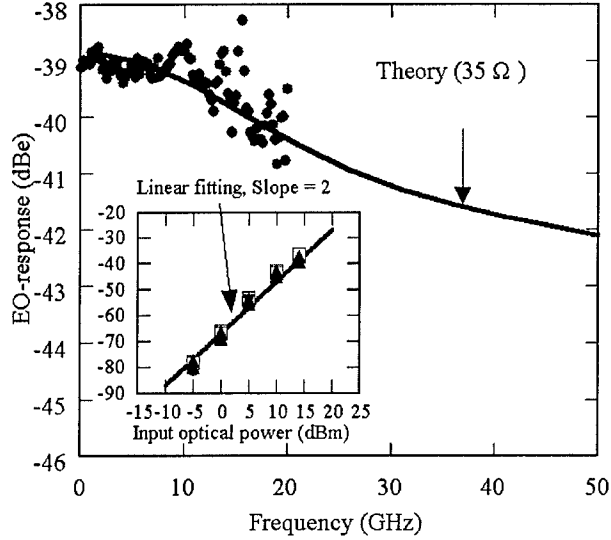
10

Figure 1.11. Frequency response for theoretical curve (solid line) and the experimental curve (points). The insert is the plot of the relative EO response with input optical power at the frequencies of 0.13,2.5,5,10,12.5,15,17.5 and 20GHz, while the line is a linear fit with slope=2.

In order to examine the capability of handling the input optical power, high-speed modulation is measured against the estimated different power levels into device (-5 dBm, 0 dBm, 5 dBm, 10 dBm, 14 dBm). The insert of Figure 1.11 shows the relative EO response as function of input optical power, while the data points are chosen at frequencies of 0.13, 2.5, 5, 10, 12.5, 15, 17.5, and 20 GHz. Similar responses (transfer function) as Figure 1.11 for different pumping levels are obtained, while the measured data was within 2 dB for each level. The 2 dB penalty is mainly due to the fluctuation from the instrument at high frequency (shown in Figure 1.11). The relation of the EO response and the input power is linear with slope of 2, suggesting that there is no significant degradation (within 2 dB) of frequency response associated with the effects of electron-hole pile-up or the photocurrent effect on the high optical power excitation. Because of the high optical loss of this device, the EO response is low (insert of Figure 1.11). However, it can be improved by high optical input power.

To further investigate the traveling wave structure, sinusoidal driven optical short pulses were generated to test the device. Two configurations of the measurement were compared: copropagating optical signal and microwave (co-direction), and optical signal and microwave propagating in opposite directions (counter-direction). The two CPW lines of the device were connected by two high-bandwidth (>40 GHz) probes, while one is terminated by a 50 Ω resister, and the other was connected by a 40 GHz sinusoidal electrical signal with $V_{p\text{-}p}$ = 5.6 V (measured by a 50-Ω load). The optical power is 2 dBm at the wavelength of 1555 nm. The output optical pulses were amplified by EDFAs and then sent to an autocorrelator for measuring pulsewidths.
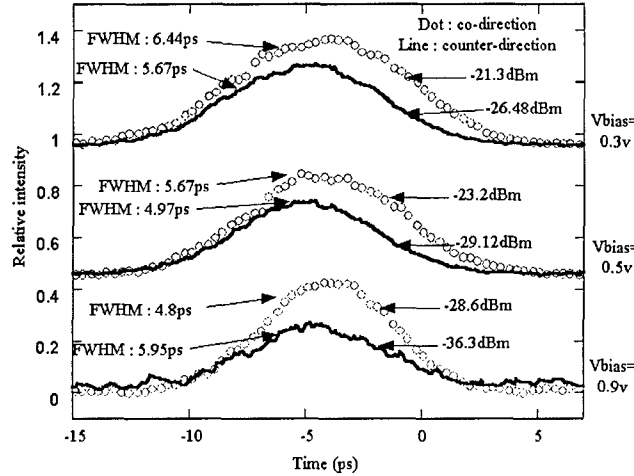
11

Figure 1.12. Autocorrelator traces of co- and counter- directions for different bias. At bias = 0.9 V, the power of counter-direction is so low that the pulse needs to be taken by a higher scale than in co-direction.

Figure 1.12 plots the autocorrelated pulses for biases 0.3, 0.5 and 0.9 V, while Table 1 summarizes the output power (before being amplified by EDFAs) and pulse widths of FWHM for different biases. The amplitudes and output power of co-directional pulses are significantly higher than those of the counter-direction. As seen in Table 1, increasing the bias causes larger differences, specifically, the power penalty due to counter-direction reaches as high as 8 dB when the bias is 0.9 V. Both counter- and co-direction measurements are the same if this were a lump element. However, the change in the output power indicates that the electroabsorption interaction in this device can only be explained by distributed effects along the long waveguide. Two main factors effect the output optical power and pulsewidths: the walk-off time and the time-gating window generated by the microwave wave along the waveguide. The waveguide length is about 1/5 of the microwave wavelength (index ~ 5.5, at 40 GHz), implying that the propagation wave behavior can not be neglected. Because the electro-optical interaction happens in the sharp on-off modulation regime (bias = 0 V to 2 V in Figure 1.10), the time-switching window becomes narrower as the bias increases, therefore the output optical pulses are very sensitive to the walk-off time relative to the microwave. Obviously, the higher walk-off for the counter-direction case than the co-direction case would result in the lower output power. And the pulses might be shortened by deterioration of the average optical power. At lower bias (<0.7 V) narrower pulses are observed in counter-direction. Due to the time-switching window changes with the bias, as can been seen in Table 1, the pulses for the counter-direction become wider as bias >0.7 V. In the extreme case, when biased at 1 V, the output power for the counter-direction case is so small that the autocorrelated trace cannot be measured, while the optical pulse width of 4.5 ps (bias = 1 V) was achieved in the co-direction case. This measurement for co- and counter-directions suggests that the traveling wave structure have the advantage to generate short pulses with higher output power.

12

Bias (v)	Power (dBm) Co-direction/Counter-direction	Pulse width of FWHM (ps) Co-direction/Counter-direction
0.3	-21.3 / -26.48	6.44/5.67
0.5	-23.2 / -29.12	5.67/4.97
0.7	-25.4/-32.4	5.04/4.83
0.9	-28.6 / -36.3	4.8/5.95
1	-30.8 / ?	4.5 / ?

Table 1.1. Summary of optical pulses shown in Figure 1.12.

1.5 Spurious free dynamic range (SFDR)

It is well known that the third order intermodulation product can be minimized and a high SFDR can be achieved if a modulator is biased at the null point of the third derivative of the transfer curve. For EAMs, the bias dependence of the SFDR is more sensitive due to the exponential transfer function. Figure 1.13 plots the 3rd derivatives of the measured DC transfer functions of our EAM for the TM mode at different input optical powers. It is clear that there is a null point in each transfer curve and the corresponding bias depends on the input optical power. Furthermore, the 3rd order derivative decreases and the linearity improves with the increase of the input optical power. Thus, we expect that the 3rd order distortion can be minimized and a high dynamic range can be achieved by adjusting both bias voltage and the input optical power. Although tuning the input optical wavelength is also an alternative to minimize the 3rd order distortion, adjusting the input optical power is a cost-effective and simple way for this purpose. To further improve the SFDR, the 5th order distortion also needs to be reduced. If we check the 5th derivatives of the transfer curves, we do find that both 3rd and 5th order derivatives can be simultaneously zero by carefully adjusting the input optical power and the polarization.
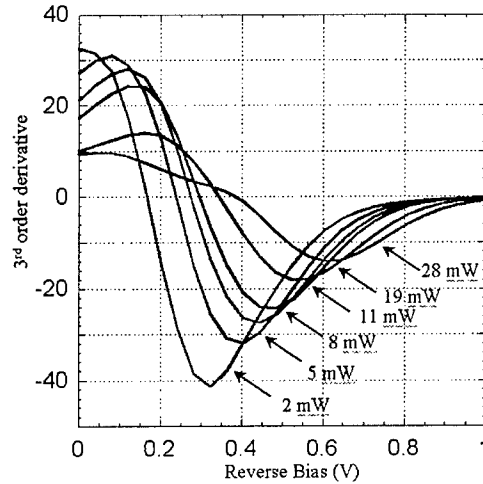

Figure 1.13. The 3rd order derivatives of the transfer function of an EAM under different input optical power.

The two-tone method was used to investigate the sub-octave SFDR of our TW-EAMs at 10 GHz. Two RF signals from synthesizers were combined and fed into a modulator. The frequencies of the two tones were set to 10 GHz and 9.9 GHz. The third-order intermodulation products were observed at 10.1 GHz and 9.8 GHz. A high-power DFB laser with wavelength at 1553 nm was used as the light source. The DFB laser had a low relative intensity noise (RIN) of ~160 dB/Hz with high power operation at 10 GHz. A highly linear photodetector was used to receive the output signals.
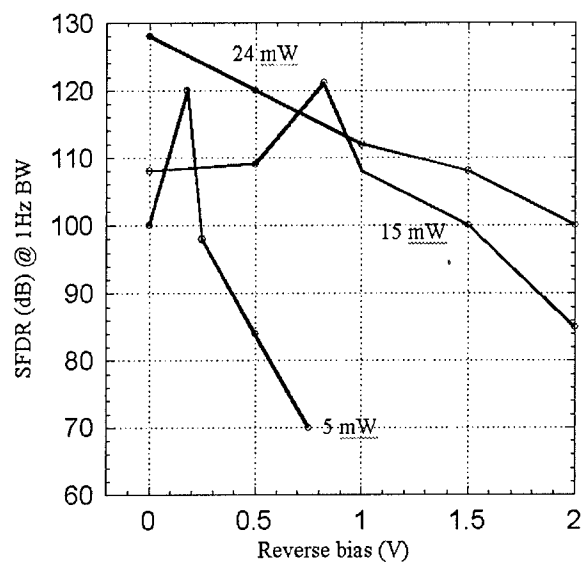

Figure 1.14. The measured SFDR in a 1 Hz bandwidth vs. different input optical powers.

The measured suboctave SFDR results at different biases and different input optical powers are summarized in Figure 1.14. By adjusting the bias voltage, 10-20 dB dynamic range improvement can be achieved. By checking the intermodulation signals, the slope of the intermodulation product *vs.* the input RF signal is 5 at the peak SFDR point, where the 3rd order derivative is zero. Figure 1.15 shows the measured fundamental and the intermodulation RF signals at three different bias points with 24 mW TE optical input power. At 0 bias, the slope of the intermodulation signal is > 5 and the highest SFDR of 128 dB-Hz$^{4/5}$ was achieved when we fit the linear curve with a slope of 5 (the best fitted curve had a slope of 6.5, and this increased the dynamic range by 5 dB). Therefore, the 3rd order intermodulation distortion cancellation was up to the sixth order power at this point. When the bias was increased to 1V, the slope of the intermodulation product was 3 and the corresponding SFDR was reduced to 110 dB-Hz$^{2/3}$. Thus, the 3rd order nonlinearity dominated the distortion. The most interesting observation here is that the dynamic range and the 3rd order derivative null point strongly depend on the input optical power level as we expected from the measured DC transfer curves. When the optical power increased from 6 mW to 24 mW, SFDR increased by 15-30 dB.
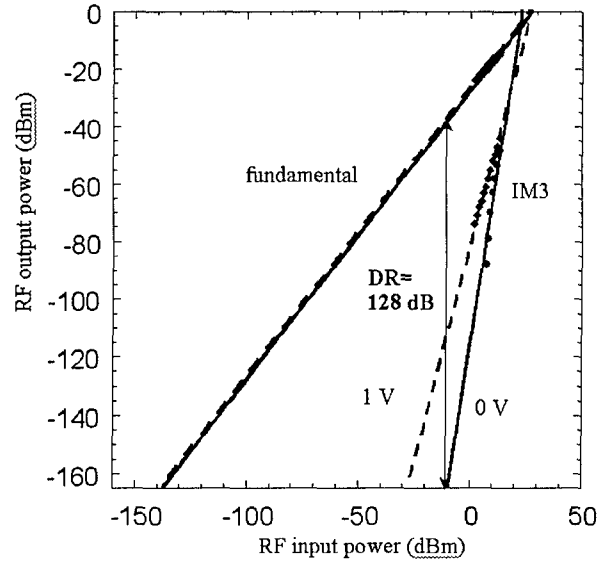
Figure 1.15. Measured fundamental and 3rd order intermodulation signals.

For an EAM with low driving voltage and high extinction ratio, RF saturation phenomena are anticipated. This is due to the nonlinear characteristic of the transfer curve. Figure 1.16 shows the RF output power vs. the RF input power under different bias voltages. Sub-linear, linear and super-linear curves are clearly observed for large RF input power, respectively. Theoretical simulations show good agreements with the experiments.
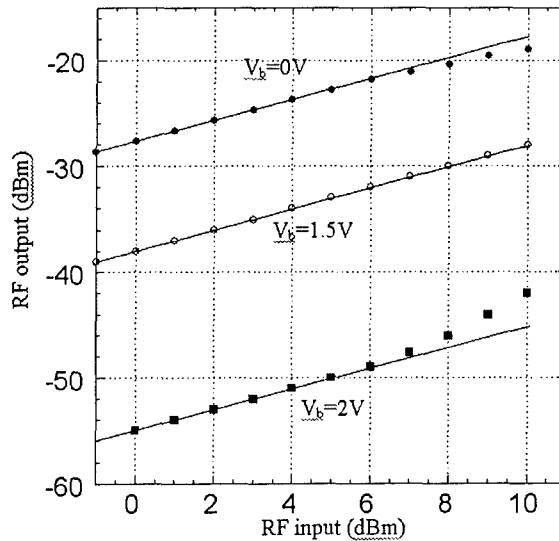

Figure 1.16. RF output power vs. RF input power under different bias voltages.

15

1.6 Link gain and SFDR with an EDFA

The simplest way to achieve link gain in an externally modulated optical analog link is to launch the input optical power as high as possible. This method has been widely adopted for Mach-Zehnder modulators. However, very high optical power is unacceptable for an EAMs, due to saturation at high optical power, heating, and the risk of facet damage. Furthermore, EAMs have high optical insertion loss due to the fact that effective QCSE happens near the band edge. Another simple way to increase the link gain is to use optical amplification. The improvement in gain comes at the cost of increased link noise figure. We have performed a link experiment with an EDFA inserted between the EAM and the detector to amplify the modulated optical signal. A tunable optical filter was placed before the detector. The link gain without an EDFA is shown in Figure 1.17 under different biases and input optical power, where the input RF signal is –10 dBm at 10 GHz. With 10 dBm optical input, the link gain is only about –40 dB. The main limitation is from the high optical insertion loss, which is about 18 dB at 0 V bias for this EAM used in this experiment. The best link gain without an EDFA for an EAM with 15 dB insertion loss is about –30 dB at 14 dBm optical input. From Figure 1.17, we also observed that the dependence of link gain on the bias is much stronger at low input optical power than at high input optical power. This is because the linearity is improved with the increase of the input optical power, however the slope efficiency is degraded and the link gain starts to saturate, which is expected from the DC transfer curve characteristics.
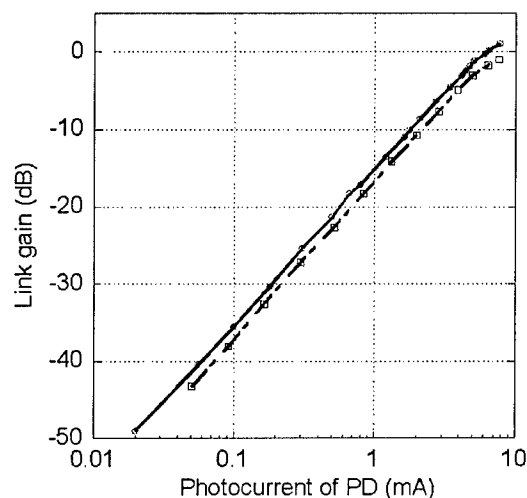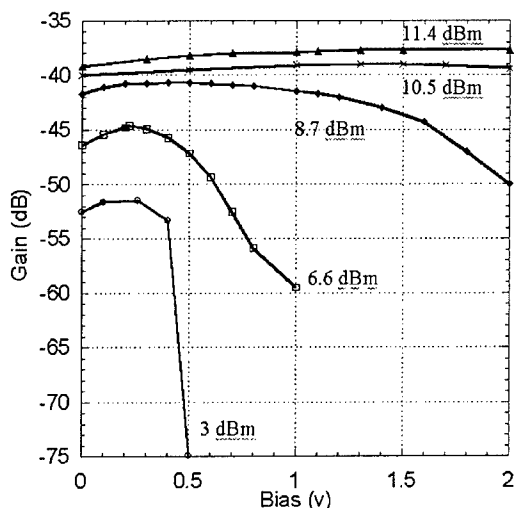

Figure 1.17. Link gain vs. bias without EDFA. Figure 1.18. Link gain versus photocurrent.

Figure 1.18 shows the link gain with an EDFA as a function of the photocurrent of the detector. The input RF signal was -26 dBm at 10 GHz, and the input optical power was about 5.5 dBm and the wavelength was 1555 nm. The bias voltage was 0.5 V for TM mode and 0.95 V for TE mode. At a photocurrent of 7 mA, the link gain reached 0 dB for TM mode, which corresponds to EDFA gain of 25 dB. A link gain of 1 dB was achieved at a photocurrent of 7.7 mA. The maximum link gain was limited by the saturation of the photodetector. Compared to the TM mode, the TE mode showed 2 dB lower link gain, due to the smaller slope efficiency for TE mode.

16

Figure 1.19 shows the measured link gain and the noise figure as a function of the EAM bias for both TM (left) and TE (right) modes. At the highest link gain of 1 dB, the corresponding NF was about 34 dB. The noise sources for a link using EDFA include the thermal noises associated with the RF generator and the receiver; the relative intensity noise (RIN) of the laser; the shot noise from the photodetector and the noise associated with the EDFA. In our link setup, the laser RIN was about 165 dB/Hz and the corresponding noise was about −160 dB/Hz. The shot noise from the PD was about −159 dB/Hz. Without the EDFA, the NF would have been about 17 dB. The signal-spontaneous beat noise from the EDFA dominated the link NF.
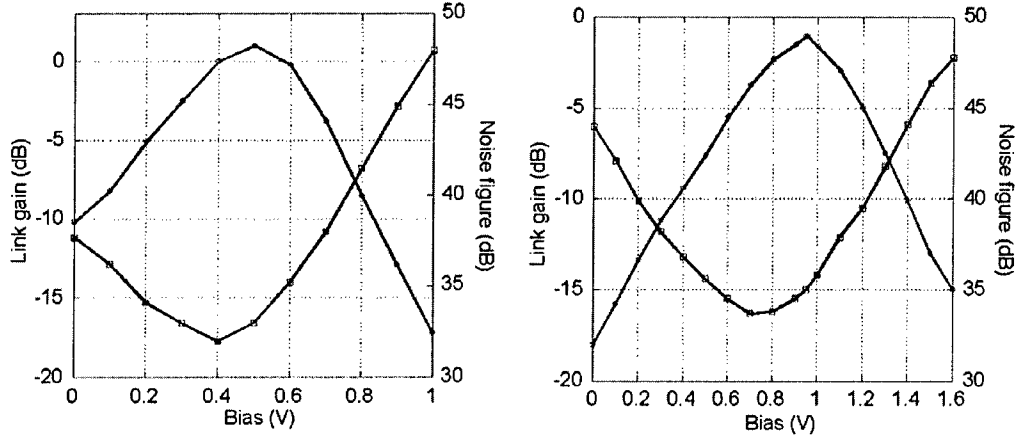

Figure 1.19. Link gain and noise figure vs. bias for TM (left) and TE (right).

The optical and RF saturation were also investigated in our link. Figure 1.20 shows the link gain vs. the input optical power. The saturation is due to the slope efficiency decrease and the saturation of EDFA and detector. Figure 1.21 shows the link gain and the RF output power as a function of the RF input power.
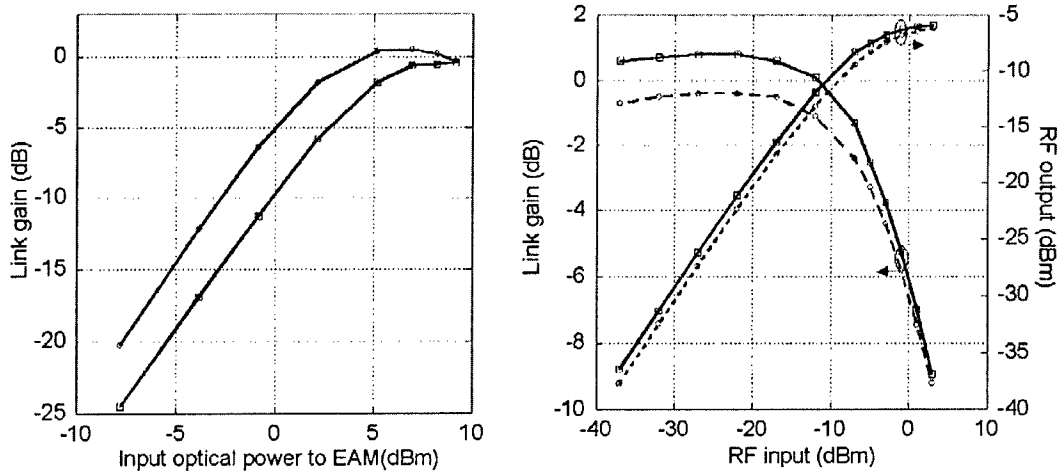

Figure 1.20. Link gain vs. optical input power. *Figure 21. Link gain and RF output power vs. RF input power.*

17

The suboctave spurious-free dynamic range was also measured for a link using a TW-EAM and EDFA. Figure 1.22 show the measured fundamental and the intermodulation RF signals at two different bias points. The bias point in the left plot corresponds to the maximum SFDR bias and the right plot corresponds to the maximum link gain bias. At the bias of 0.45 V, the measured SFDR is about 112 dB-Hz$^{4/5}$ at 1 Hz bandwidth. Thus, the 3rd order distortion has been minimized at this bias. Compared to a link without an EDFA, SFDR is decreased. This is mainly due to the noise floor is increased more than 20 dB. At the bias of 0.5 V, the link has the maximum link gain of 1 dB, however, the SFDR is decreased to 102 dB-Hz$^{2/3}$. The 3rd order distortion dominates the dynamic range here. Note that the link gain at maximum SFDR bias is only about 1 dB lower than the maximum gain, but the dynamic range improvement is 10 dB.
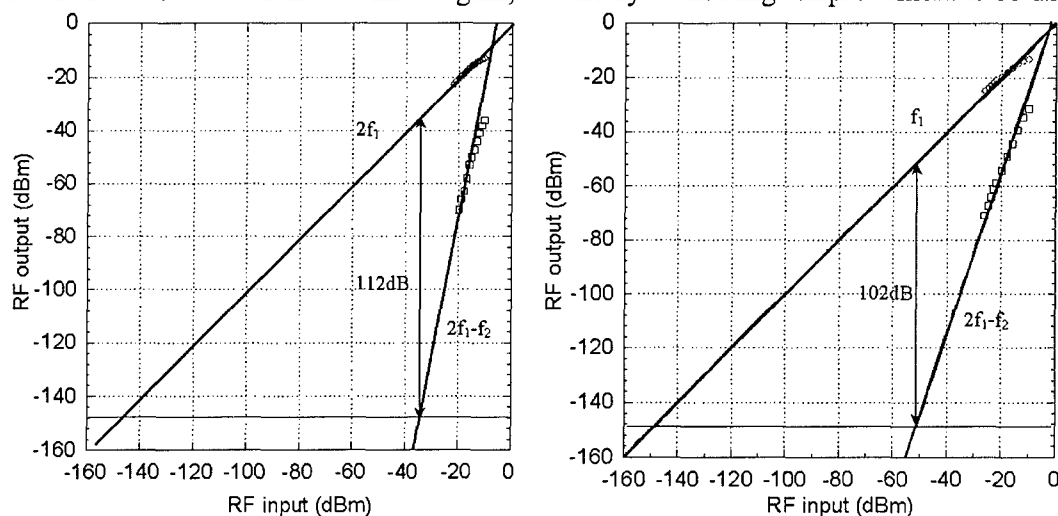

Figure 1.22. Measured fundamental and the intermodulation RF signals with the device biased at maximum SFDR (left) and maximum link gain (right).

18

2. Tunable Optical Transmitter Chip

This section of the report is organized as follows: Subsection 2.1 describes the design and fabrication technology for a widely-tunable SGDBR laser integrated with an SOA and EAM; Subsection 2.2 presents chip performance characteristics of the widely-tunable CW and EA-modulated sources; Subsection 2.3 outlines control and calibration principles and presents the performance characteristics for the calibrated modules; Subsection 2.4 presents performance characteristics of the SGDBR-SOA-MZM devices; Subsection 2.5, finally, summarizes the results.

2.1 Device design and fabrication

As illustrated in Figure 2.1.a, the device consists of a SG-DBR laser, a SOA, and an EA modulator, all integrated on the same InP chip. The SG-DBR laser includes gain and phase sections positioned between two "sampled grating" distributed reflectors. By imposing additional periodicity on holographically defined Bragg grating the reflectivity spectra of the mirrors are transformed into a comb of reflectivity peaks centered at the Bragg wavelength. The spacing between adjacent peaks, $\Delta\lambda$, is inversely proportional to sampling period defined by conventional lithography. The front and back mirrors of the laser are sampled at different periods such that only one of their multiple reflection peaks can coincide at a time, as shown in Figure 2.1.b (This is known as the Vernier effect). Introducing a small index change in one mirror relative to the other causes adjacent reflectivity maxima to come into alignment, shifting the lasing wavelength a large amount for small index change. Continuous tuning between the reflectivity maxima is obtained by tuning both mirrors. Biasing of the phase section fine-tunes the effective Fabry-Perot cavity mode into alignment with the maximum reflectivity of the mirrors. The tuning range of a SG-DBR laser is defined by the repeat mode spacing and can be designed to exceed the tuning range of a conventional DBR laser by a factor of 10. The wide tuning range of SG-DBR lasers does not compromise side-mode suppression since several narrow passbands are used instead of a single wider passband filter tunable over a wide range [1].
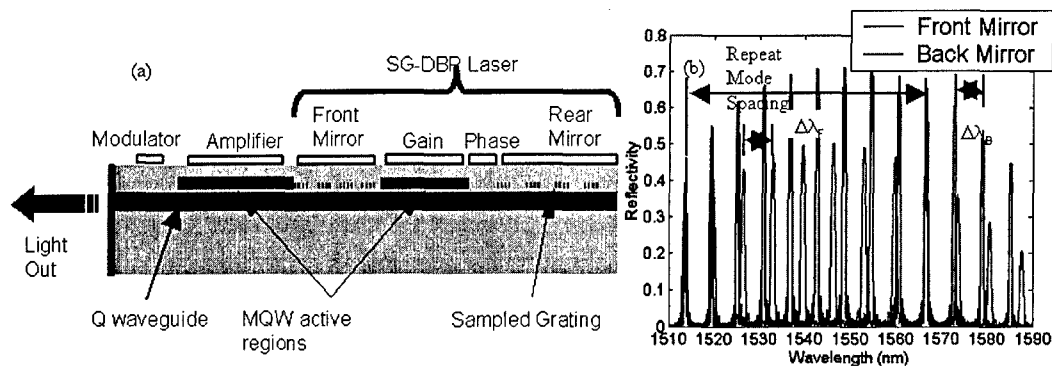

Figure 2.1: (a) Schematic of an SG-DBR laser integrated with an SOA and a modulator, (b) Reflectivity spectrum of the sampled grating mirrors showing the multiple mirror peaks used to cover the tuning range.

19

The integrated SOA compensates on-state modulator loss and cavity losses caused by free carrier absorption in the tuning sections and allows wavelength independent power leveling. The integration of the laser and SOA active regions with the tuning and modulator sections of the device has been accomplished by using an offset quantum-well structure. In this simple integration technology the bulk quarternary waveguide and multi-quantum well (MQW) active region are grown in one MOCVD step, then the MQW material is selectively removed from the modulator and tuning sections of the laser and the sampled grating is defined using conventional lithography and holography. Next, InP p-cladding is regrown and a shallow ridge structure is formed using a combination of dry and wet etching. Finally, the ohmic contacts are formed for each section of the device.

The described fabrication process is exactly the same as the process used for fabrication of a SGDBR laser alone. Hence, the integration with the SOA and modulator does not introduce additional processing steps allowing for high-yield manufacturing.

In this technology the active region of the modulator uses the same bulk quaternary waveguide as the tuning sections of the laser. The Franz-Keldysh effect in the bulk waveguide material provides for larger spectral bandwidth as compared to the quantum-confined Stark effect. The cross-sectional design of the structure was optimized for high tuning efficiency for the laser and target transfer function and modulation bandwidth for the modulator using the following optimization parameters:

1) Band-gap of the quaternary waveguide
Narrower band-gap of the waveguide results in higher index tuning efficiency under forward bias and higher modulation efficiency under reverse bias. The trade-off is insertion loss in the laser and modulator structures.

2) Thickness of the quartenary waveguide
The optimum thickness of quaternary waveguide was determined based on the confinement factors for the laser and SOA gain sections and the tuning sections of the laser.

3) Doping distribution in the waveguide
The optimized waveguide thickness is larger (~0.3 μm) than the optimum for the depletion region of the EA modulator (~0.2 μm). This was corrected by introducing a split-doping approach in which the lower 0.1 μm of the waveguide was doped n-type.

The longitudinal optimization of the chips addressed SOA, EAM, and output coupler designs. The SOA was optimized for high saturation power at typical drive current levels of 150-200 mA. This was accomplished by optimizing SOA length and shape (taper) using modeling software developed by Agility. The modulator design was optimized for the target modulation bandwidth and high power handling capability by optimizing device length and thickness and shape of the Au-plated electrodes.

Finally, the angled and tapered output coupler was optimized based on the trade-off between the output facet reflectivity that can be dramatically decreased by widening the ridge and shape of the far field (FF) that determines the coupling efficiency into the fiber. Figure 2.2.a shows reflectivity from an uncoated facet for 4 and 6 μm wide output waveguides. Reflectivity below 4×10^{-4} can be easily achieved for 6 μm wide ridge at ~7 degree angle. However, wider ridge results in narrower horizontal FF angle and, hence, more asymmetric FF and lower CE as illustrated in Figure 2.2.b.
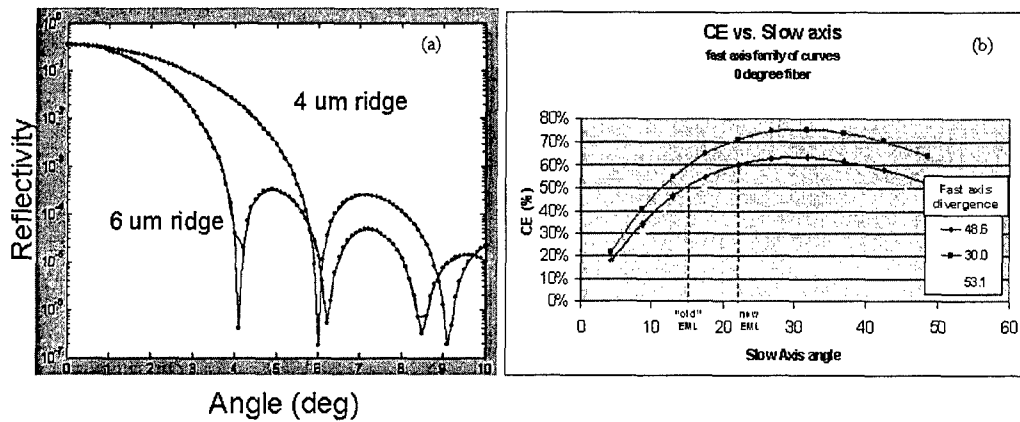
Figure 2.2. (a) Reflectivity as a function of output waveguide angle, (b) Calculated coupling efficiency to an optical fiber.

2.2 Chip performance characteristics

Figure 2.3 presents ex-facet output power for a SGDBR-SOA chip mounted on ceramic carrier. More than 50 mW of power is demonstrated for 150 mA drive current for the gain and SOA sections. The output power across 50 nm tuning range can be further increased to 80 mW by increasing the SOA current to 280 mA.
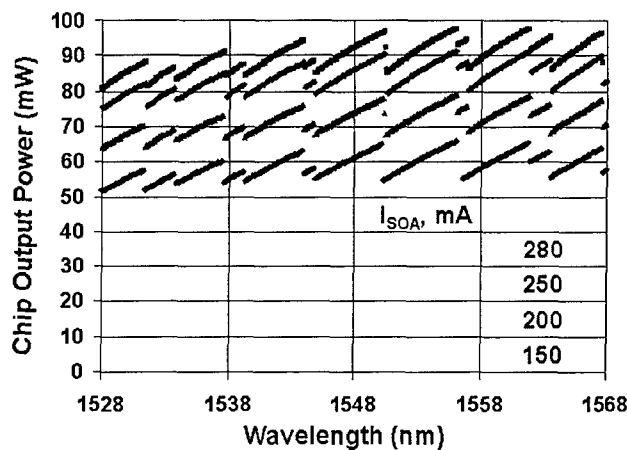

Figure 2.3. SDGBR-SOA ex-facet power as a function of waveleng for several values of the SOA current. Gain current is kept at 150 mA.

Figure 2.4 presents performance characteristics of an SGDBR-SOA-EAM chip. For this integrated device the band-gap wavelength of the quaternary waveguide was red shifted to 1.43 nm to achieve target modulation efficiency across 40 nm tuning range. As a result, the increase in the propagation loss throughout the device leads to some reduction of chip output power as compared to CW optimized SGDBR-SOA chips. However, 30-45 mW ex-facet power is still achievable for 150 mA currents applied to the gain and SOA section and 0 V on the modulator section.
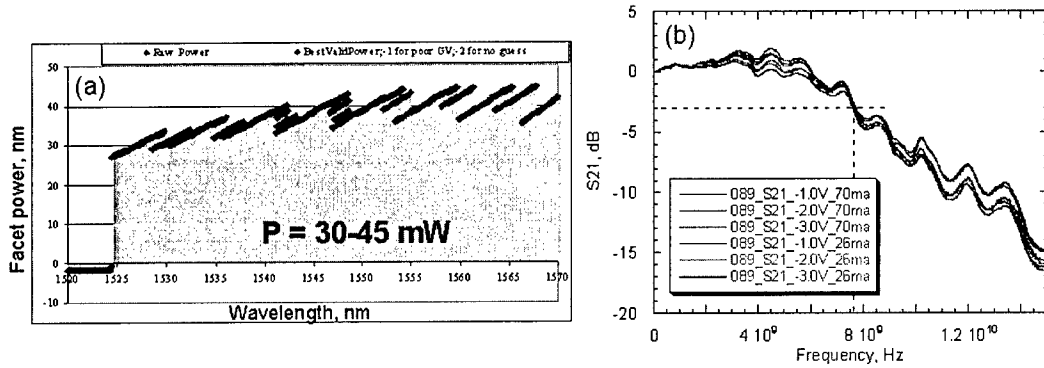
21

Figure2.4. (a) Ex-facet output power for a SGDBR-SOA-EAM chip under $I_{gain} = I_{SOA} = 150$ mA and $V_{EAM} = 0V$; (b) small signal modulation response of an EAM at several reverse bias conditions and several values of input optical power (SOA current).

Modulator small signal modulation bandwidth, measured at several reverse biases on the modulator and several values of input optical power (several values of the SOA current), is presented in Figure 2.4.b. The measured –3 dB bandwidth exceeds 7.5 GHz. The bandwidth is not dependent on the bias condition indicating that the active region of the modulator is fully depleted even under low biases. The bandwidth also does not show significant dependence on the input power confirming that the carrier pileup is not a problem for these bulk modulators.

Since the input optical power for the integrated EAM is relatively high (up to 50 mW), special development efforts were devoted to optimization of the devices for power handling capability. The electroabsorption modulator experiences the strongest thermal effects of any section in the integrated device. This is due to a positive feedback cycle that is created: as incident light is absorbed in the modulator, Joule heating occurs due to the applied voltage and the photocurrent that is produced. This heating causes a local reduction in bandgap, which in turn increases absorption, causing additional heating. This effect will be strongest at the front of the device, where the optical power is high.

The optimization cycle included detailed experimental and theoretical analysis of the temperature distribution for the initial EAM design followed by the optimization of the modulator contact pad thickness and geometry and experimental verification of the improved power handling capability. Experimental measurements were performed using a thermal imaging technique based on thermoreflectance. This thermal imaging system has achieved submicron spatial resolution and < 0.1°C temperature resolution; details of the measurement technique and initial results are described in reference [2]. Figure 2.5 shows images of the EAM device under operation; significant heating localized at the front of the modulator is clearly evident.

A finite-element thermal model was developed for comparison to the experimental results. This one-dimensional model calculates optical power absorption, local photocurrent, and local temperature self-consistently using the Varshni equations for thermal bandgap shrinkage. Thermal impedance values are calculated from a detailed analysis of the ridge cross-section. Figure 2.5.c shows measured and calculated thermal profiles at low input power, along the longitudinal axis of the unoptimized EAM. Excellent agreement is obtained between the calculated and measured distributions. Figure 2.5.c compares the bias dependence of the peak temperature under high optical

22

input power (~ 35 mW at 1548 nm) for the two different modulator designs. The unoptimized design clearly exhibits thermal runaway at ~ 2.75 V, with very high surface temperatures indicated. In contrast, the optimized structure, using the same epitaxial layer structure, exhibits much lower heating and can be operated to higher voltages without triggering thermal runaway. These optimized devices consistently achieve damage-free operation at a DC bias of 5 V and well over 60 mA photocurrent (total electrical power in excess of 300 mW).
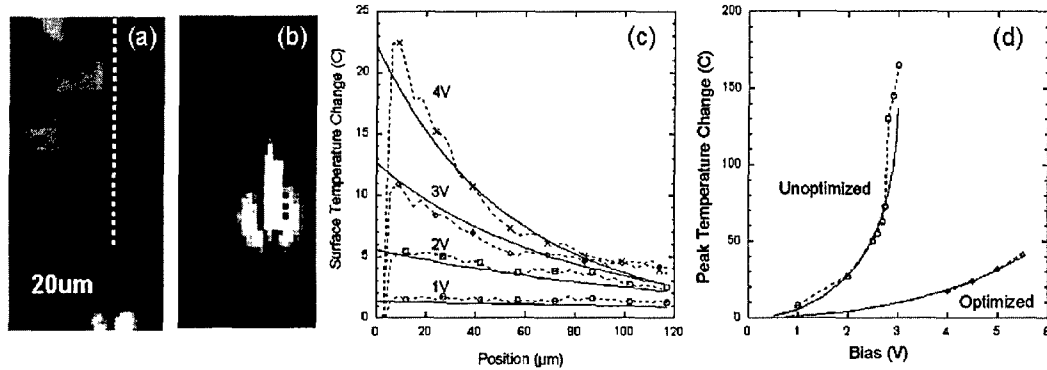

Figure 2.5. Optical (a) and thermoreflectance (b) images of an EAM; (c) Surface temperature rise along the ridge: thermoreflectance measurement (dashed line) and model (solid line). Input power is ~ 6 mW, and operating wavelength is 1548 nm. (d) Maximum temperature as a function of modulator bias: thermoreflectance measurement (dashed line) and model (solid line). The input power is around 35 mW, and operating wavelength is 1548 nm.

Final optimization of the integrated SGDBR-SOA-EAM chip addressed output coupler design. Devices with two values the ridge waveguide widths at the output facet were fabricated packaged and characterized. Typical coupling efficiency for the wider output waveguide was below 45 % while the measured coupling efficiency and standard deviation for the narrower waveguide were 53.8% and 2.6%, respectively. These results are consistent with target 10% improvement in coupling efficiency (see Figure 2.2.b). Figure 2.6 shows that optimized SG-DBR-SOA-EAM chips are capable of producing more that 15 mW of fiber-coupled power for gain and SOA currents of 150 mA.
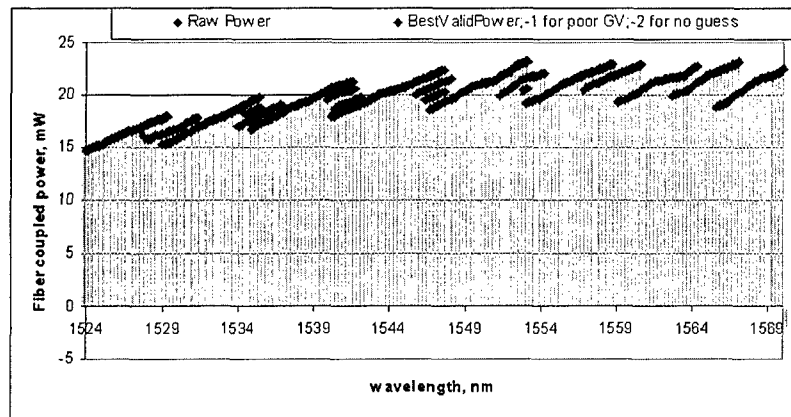

Figure 2.6. Fiber-coupled power for SGDBR-SOA-EAM device across 46 nm tuning range. $I_{gain} = 150\ mA$, $I_{SOA} = 150\ mA$, $V_{EAM} = 0V$.

23

2.3 Packaging and control algorithms

2.3.1 Laser Diode Module (LDM)

The integrated SGDBR-SOA-modulator chips and a multi-channel wavelength locker were mounted into a cooled butterfly module with a co-planar RF input Figure 2.7 presents a schematic showing the concept for integrating the wavelength locker into the LDM and fully functional LDM prototype.
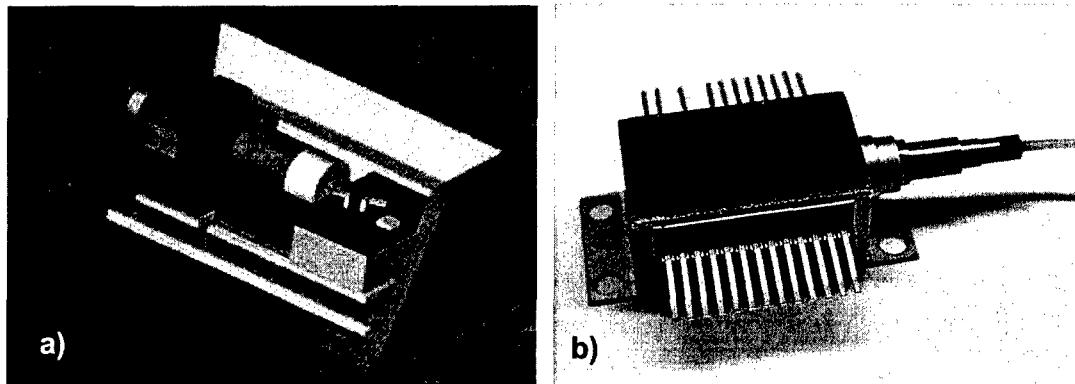

Figure 2.7. a) Schematic drawing of the wavelength locker assembly integrated into the LDM; b) Package widely-tunable optical transmitter based on SGDBR-SOA-EAM chip.

The main criteria for the locker sub-assembly is that it must provide a stable frequency lock point (+/- 3 GHz) over temperature and life while maintaining a small size that can be co-packaged with the laser in the industry standard footprint (1.2" x 0.5" x 0.4"). The concept developed to achieve this is shown in Figure 2.8. The wavelength locking subassembly is inserted into the package between the lens that collimates the laser light and the lens that focuses this light into the fiber. The locker taps off two
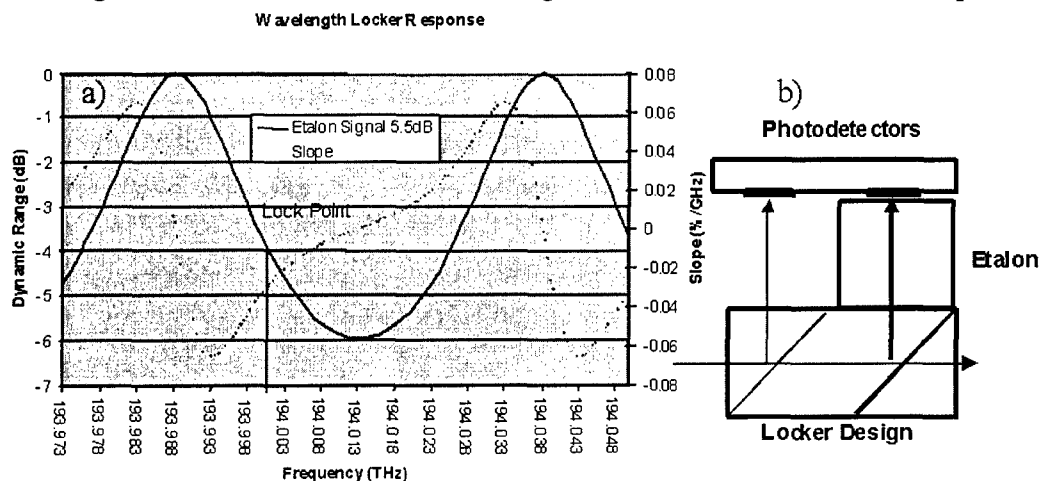

Figure 2.8 a) The transmission response of a Fabry-Perot etalon showing how the reference and etalon photocurrents can be compared to derive a lockpoint; b) Schematic concept of the wavelength locking assembly that illustrates the beam splitters, etalon and photodetectors.

24

portions of the light and directs them to two photodetectors. The Fabry-Perot etalon lies in one of the paths to the photodetectors, providing a wavelength sensitive photo-response. By comparing the photocurrent of the two detectors, the lock point for each channel can be established at a particular slope on the etalon response as shown in Figure 2.8.a.

2.3.2 Control algorithms and calibration procedures

Electronically-tunable lasers like SGDBR lasers require the coordinated injection of current into more than one tuning section (see Figure 2.9). Control of an SGDBR laser is intimately connected to its principle of operation. Each of the sampled grating mirrors exhibits a multi-peaked reflectance spectrum. Mirror tuning current shifts a mirror's reflectance spectrum to shorter wavelengths by a controlled amount, and because of the Vernier effect, only a single set of peaks have significant overlap for any given amount of tuning. In conjunction with this, there exists a cavity mode spectrum that describes which possible wavelengths satisfy the round trip phase condition necessary for laser oscillation. The combination of mirror tuning currents with best overlap selects the cavity mode at which lasing occurs, the phase tuning current fine-tunes the cavity mode's wavelength, and the gain section current controls the output power.
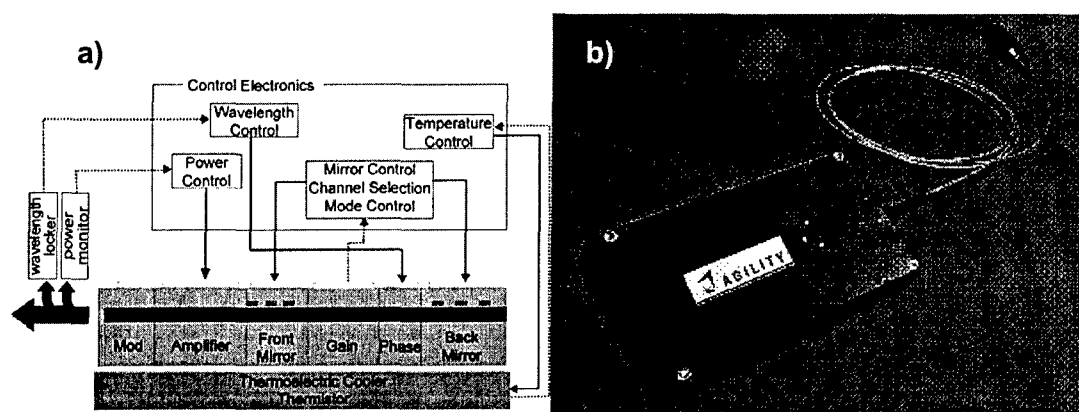

Figure 2.9   a) Schematic Diagram of an SGDBR laser with feedback and control system. b) Tunable laser assembly.

Because of variations in the fabrication process, the tuning currents to achieve a particular wavelength are slightly different for each fabricated laser, so that each laser must be properly calibrated before installation. Additionally, the extinction ratio (ER) characteristics of EA-modulators are strongly dependent on the detuning between the lasing and absorption-edge wavelengths. To provide uniform RF ER over a wide spectral bandwidth, the dc and modulation bias on the modulator section has to be adjusted for each channel.

Robust calibration and control algorithms have been developed and implemented in hardware and firmware. Figure 2.10 presents power, frequency deviation, and SMSR for a calibrated TLA. The power variation between the channels is less than +/- 0.1 dB. Frequency accuracy is better that +/-1 GHz over 0 + 70C temperature range. SMSR is better than 40 dB.
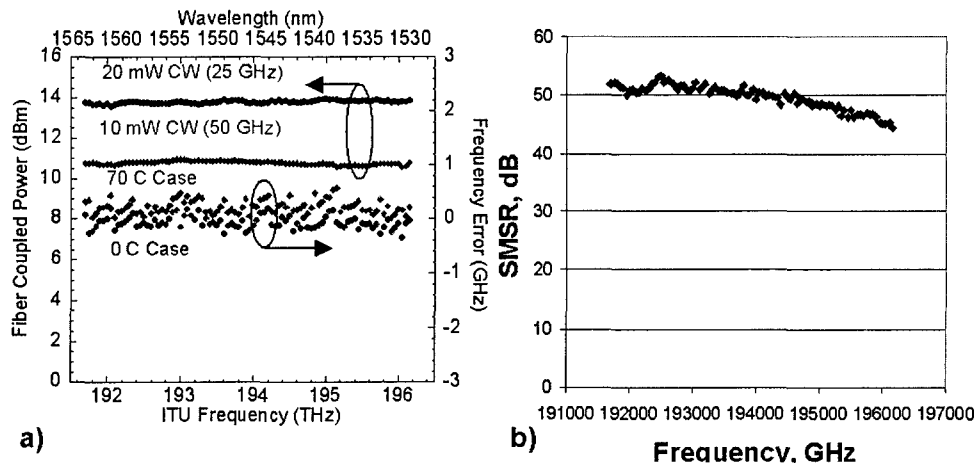
25

Figure 2.10. Characteristics of a calibrated TLA: (a) Output optical power for a TLA calibrated for 10 and 20 mW and frequency deviation at 0 and 70 C case temperature; (b) side mode suppression ratio.

2.3.3 Modulator Calibration

The calibration procedure developed for the modulator biases relies on dc ER measurements during calibration of the tunable laser assembly. The developed procedure eliminates time consuming and expensive multiple RF tests. Figure 2.11. b shows measured dc ER for 87 ITU channels. The dc ER is a smooth function of wavelength and dc voltage. The algorithm for selecting modulator bias conditions (dc bias V_{dc} and peak-to-peak modulation voltage V_{pp}) is illustrated in Figure 2.11.a. Measured dc ER curves are fitted with the third order polynomial and on-state modulator bias is selected for each channel using constant slope criterion. Next, V_{pp} is calculated using target value of dc ER. The resulting V_{dc} and V_{pp} settings as function of wavelength are shown in Figure 2.12 a. The RF ER measured for a calibrated tunable electroabsorption modulated laser assembly (TEMLA) is shown in Figure 2.12.b. RF ER > 10 dB and time-averaged output power > 5 dBm can be maintained across 40 nm tuning range. Similar calibration approach for an electroabsorption modulator can be implemented to achieve uniform analog characteristics across the wide tuning range of the device.
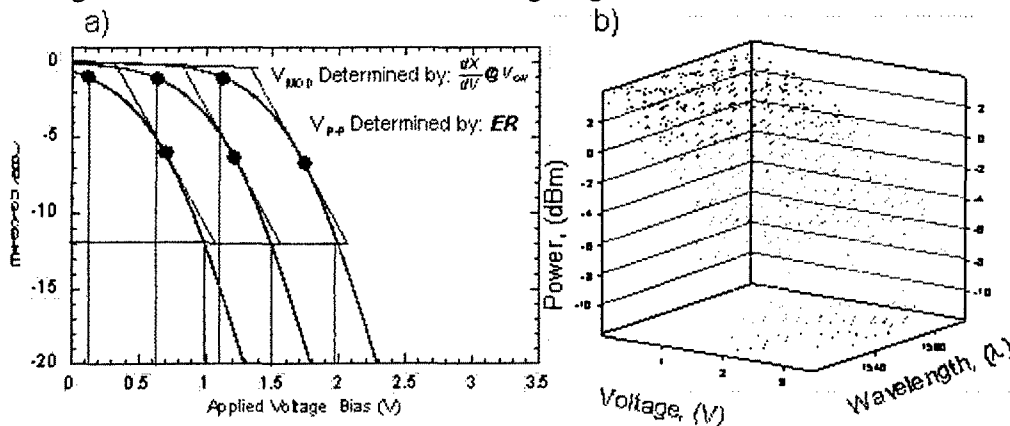

Figure 2.11. a) Schematic of dc ER curves for three wavelength as a function of dc bias on the modulator section; b) Measured dc ER for 87 ITU channels.
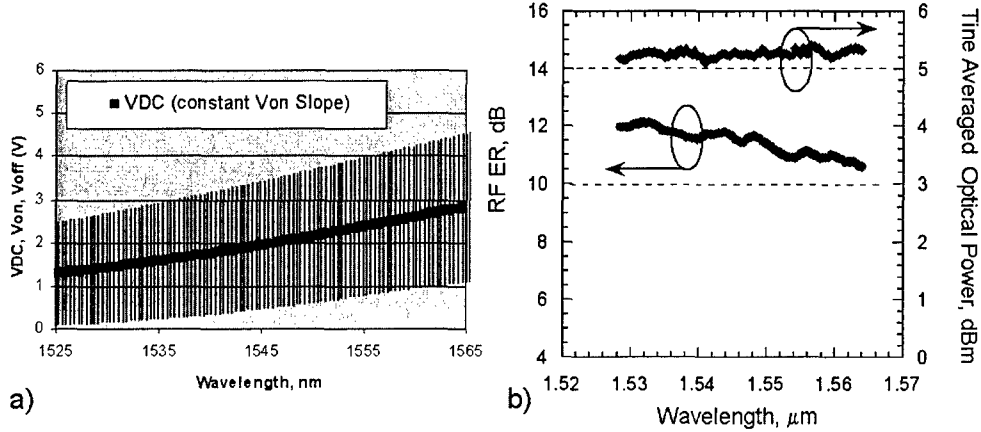
26

Figure 2.12 a) Voltage settings extracted from measured dc ER curves; b) Measured RF ER and time-averaged output power across the tuning range.

2.4 SGDBR-SOA-MZM performance characteristics

As will be detailed in the part of the report devoted to the analog characteristics of the developed devices, the available RF gain of the EA modulators is limited by the generated photocurrent. In contrast to the electroabsorption modulators, Mach-Zehnder modulators are immune to this limitation since they are relying on electro-refractive effect with very little or no generated photocurrent. Absence of the photocurrent also leads to the additional advantages of lower dissipated power (provided that MZM V_π is comparable to the effective V_π of EAM) and increased reliability. Finally, controllable chirp of MZ modulators makes them especially attractive for high-speed fiber-optics digital transmission.

We designed and fabricated integrated chips comprising of SGDBR laser integrated with SOA and MZ modulator. The performance characteristics presented in Figure 2.13 include ex-facet power of more that 20 mW and –3dB small signal modulation bandwidth exceeding 10 GHz.
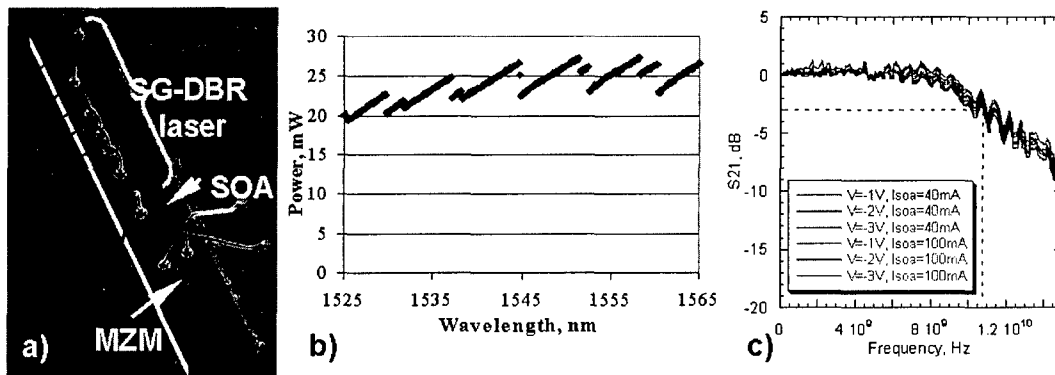

Figure 2.13. a) Scanning-electron microscope image of an SGDBR-SOA-MZM chip mounted on ceramic carrier. b) Ex-facet output power of an SGDBR-SOA-MZM chip for $I_{gain} = I_{SOA} = 150$ mA with MZM biased into transparency (zero phase shifted configuration). c) Small signal modulation bandwidth of a MZM measured at several biases and for several values of the input optical power.

27

2.5 Summary

During this project Agility Communications developed widely-tunable integrated chips suitable for realization of compact high-performance transmitters for analog and digital optical links. The developed devices tune across 40 nm wavelength range in the C-band with SMSR in excess of 40 dB. The chips optimized for CW operation are capable of producing more than 80 mW of output power. The EA and MZ modulated chips output 30 and 20 mW power, respectively. The bandwidth of the devices exceeds 7.5 (EAMs) and 10 GHz (MZMs). The digital characteristics of the EA and MZ modulated devices meet the requirements of OC-48 and OC-192 systems, respectively.

During this project Agility developed manufacturable fabrication processes and optimized the integrated chips for high optical power and power handling capability. Laser and modulator calibration procedures and control algorithms were developed and implemented in hardware and firmware. Throughout the program prototypes of developed components (chip-on-carriers (CoCs), laser diode modules (LDMs), and LDMs integrated control boards) were provided for RF experiments.

Further optimization of the integrated devices for linearity is possible by tailoring modulator transfer characteristics through incorporating multi-section modulator designs. The modulation speed of the devices can be further increased by implementing traveling-wave designs.

References:
[1] V. Jayaraman, Z.-M. Chuang, L. A. Coldren, "Theory, Design, and Performance of Extended Tuning Range Semiconductor Laser with Sampled Grating", *IEEE J. of Quantum Electron.*, vol. 29, pp. 1824 –1834, 1993.

[2] Z. Bian, J. Christofferson, A. Shakouri, P. Kozodoy, "High-Power Operation of Electroabsorption Modulators," Appl. Phys. Lett., Vol. 83, pp. 3605-3607, 2003.

3. Analog Characteristics of Optical Transmitters

3.1. SG-DBR laser noise performance

Two types of optical transmitters were investigated in this work. The device used for most of the work described within this paper consists of a SG-DBR laser, a SOA, and an EA or MZ modulator, all integrated on the same InP chip, as illustrated in Figure 3.1. The second type of device consists of a stand-alone SG-DBR laser. This device was used mainly for some of the investigations into the RIN performance of the SG-DBR lasers, decoupled from the added noise from the SOA, and also for investigating the direct modulation response of the SG-DBR laser. It will be clearly stated within the report when the stand-alone SG-DBR laser was used for characterization.
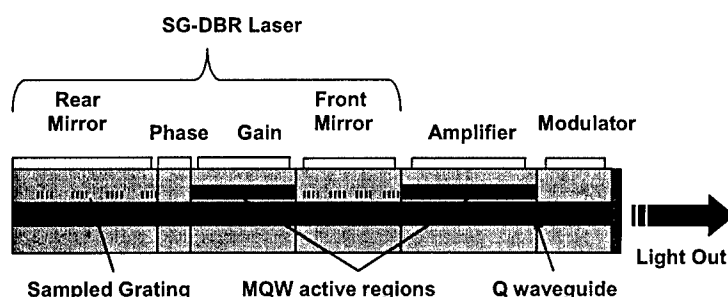

Figure 3.1. SGDBR-SOA-EAM Device Schematic

The relative intensity noise (RIN) is produced both in the SG-DBR laser structure and, when integrated, in the SOA section. Figure 3.2 shows the measured RIN spectra for an SG-DBR laser integrated to an SOA, for different values of gain section bias. The SOA bias was fixed at 180 mA. At 200 mA, the peak RIN is lower than −153 dB/Hz. The detector shot noise contribution has been subtracted in these graphs. Figure. 3.3 shows the RIN for different values of bias applied to the SOA. The gain section bias was here fixed at 180 mA. The RIN improves with increasing SOA bias as expected, being minimum in the 120 mA to 140 mA range, after which increased heating slightly degrades the noise performance. The noise performance of the SOA noise is best observed at frequencies away from the laser RIN peak, particularly below a few GHz, where the overall noise is limited by the SOA spontaneous emission. This effect is also confirmed in Figure 3.2 by the compression of RIN level around 2 GHz for gain section bias higher than 100 mA.
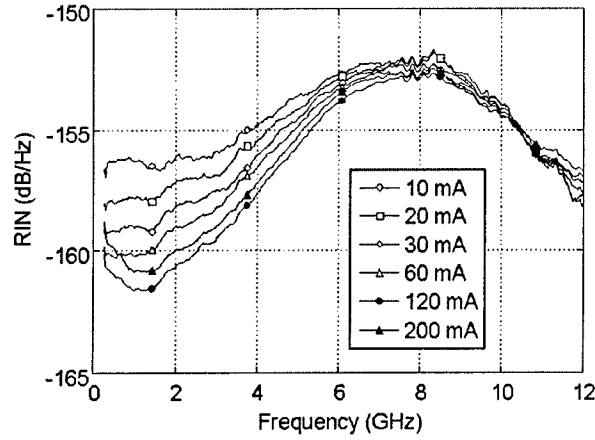
29

Figure 3.2. Detected RIN spectra at 1552 nm for different values of gain section bias. SOA bias fixed at 180 mA.
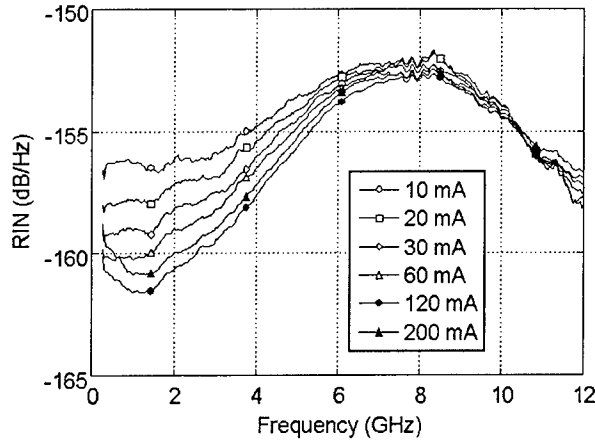

Figure 3.3. Detected RIN spectra at 1552 nm for different values of SOA bias. gain section bias fixed at 180 mA.

The RIN of the stand-alone SG-DBR laser is shown in Figure 3.4. The RIN is taken at 0.2 GHz as a function of the fiber-coupled output power of the laser when only the gain section is biased. At low bias current, the system RIN is inversely proportional to the cube of the optical power, which means it is dominated by the laser source noise. It is seen that without the integrated SOA, the projected RIN noise of the SG-DBR laser at high output power is indeed below −160 dB/Hz at higher output power, confirming that the noise performance of the SG-DBR laser, integrated with an SOA, shown in Figure 3.2, is limited by SOA noise below 2 GHz.
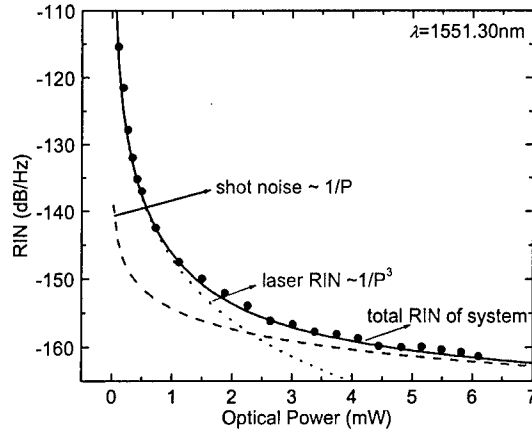
Figure 3.4. RIN taken at 0.2 GHz vs. optical power while only the gain section of the SGDBR laser is being biased.

An investigation of the SGDBR laser noise properties over the tuning range is provided by Figure 3.5, showing the fiber-coupled optical power and the corresponding RIN plus shot noise performance of ten channels for the stand-alone SG-DBR laser. It indicates uniform RIN properties, here limited by the photodiode shot noise along the whole tuning range, inversely proportional to the optical power. The reduction of power at some channels is due to the absorption loss induced by the high mirror currents. The worst RIN is below −155 dB/Hz for the channel having lower output power around 3 dBm. There is only a slight RIN increase at the mode-hop boundary, which is due to the decrease of the output power. Further examination of the RIN spectra shows that the resonance frequency also varies with the output power of different channels. The linear relation between the resonance frequency and the square root of the output power is also valid. While the output power of these channels vary from 3 dBm to 7.3 dBm, the resonance frequency varies from 3.5 GHz to 5.5 GHz correspondingly.
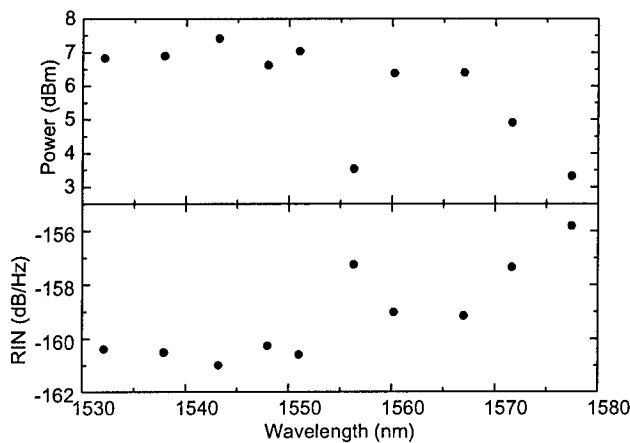

Figure 3.5. Fiber-coupled optical power and the corresponding RIN values at 0.2 GHz, of ten optimized channels along the >45nm tuning range.

31

3.2. Direct modulation: SG-DBR laser

The direct modulation response of the SG-DBR laser is characterized using an SG-DBR laser, not integrated to an SOA or EAM. Figure 3.6 shows a typical small-signal direct intensity modulation response of the SG-DBR laser as a function of applied gain section bias. The resonance frequency of the SGDBR can be obtained from the peak of the modulation response as shown in Figure 3.7. Also seen in the plot is the resonance frequency determined from the RIN peak of a stand-alone SG-DBR. It can be seen that these two plots agree well and their slope is approximately equal to 1.5 GHz/mA. This overlap of the two characteristics indicates that the effect of parasitic elements on the modulation bandwidth is negligible up to 4.8 GHz. The maximum achievable, damping-limited modulation bandwidth can be estimated by parameter extraction from either curve-fitting the RIN spectra or the direct modulation response. In both cases, a damping-limited modulation bandwidth about 15 GHz is obtained.
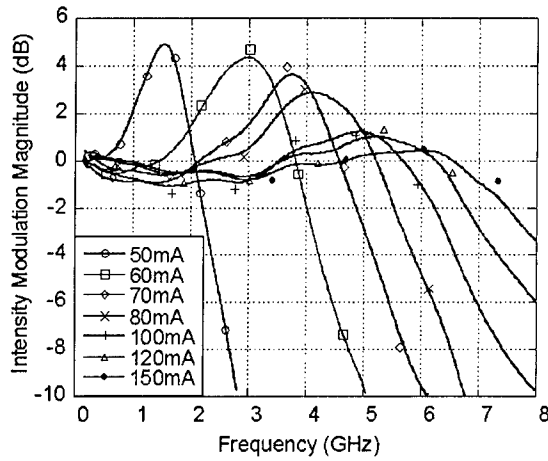
Figure 3.6. Small signal direct intensity modulation response of the SG-DBR laser as a function of gain section bias current.
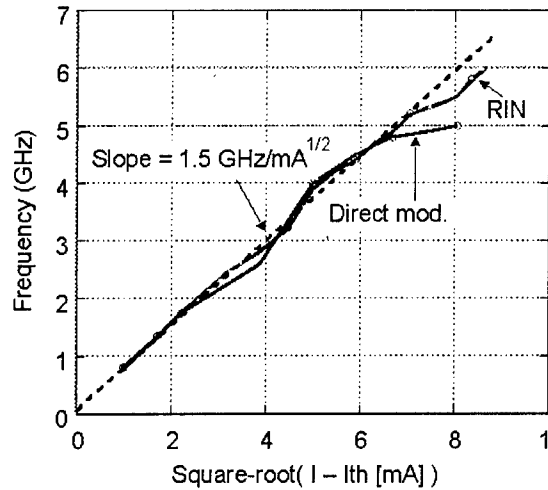
Figure 3.7. SG-DBR resonance frequency obtained from the RIN peak and the peak in direct modulation response, as a function the square-root of above threshold gain section bias current.

32

Dynamic range: The spurious-free dynamic range (SFDR) of the directly modulated, stand-alone SG-DBR laser is characterized by the two-tone method. Figure 3.8 shows the power of fundamental and third order distortion products from the directly modulated SG-DBR laser biased at 60 mA, using two modulation tones at 0.5 GHz, separated by 1 MHz. Also shown is the noise floor at −160 dBm/Hz, limited by receiver shot noise. The SFDR is about 112 dB/Hz$^{2/3}$ and the input power of the 3rd order intercept point, IIP3, that is higher than 25 dBm. Figure 3.9 shows the IIP3 and SFDR values of the laser versus the bias current of the gain section. The figure shows that there is an optimized bias current, around 55 mA, where the best distortion properties are found. This is due to the compromise between the threshold current and the thermal roll-off of the L-I curve at high bias current. The SFDR value is always above 110 dB/Hz$^{2/3}$ and the IIP3 is above 22 dBm. The same measurements were done for modulation bandwidths from 0.1 GHz to 5 GHz, where the SFDR remains above 100 dB/Hz$^{2/3}$ and the IIP3 above 20 dBm over the frequency range. The input power of the 2nd order intercept point, IIP2, is always higher than 20 dBm, measured by single tone modulation. Similarly, the SFDR and IIP3 is always above 100 dB/Hz$^{2/3}$ and 20 dBm over ten wavelength channels covering the tuning range of the SG-DBR, measured at 120 mA gain section bias current.
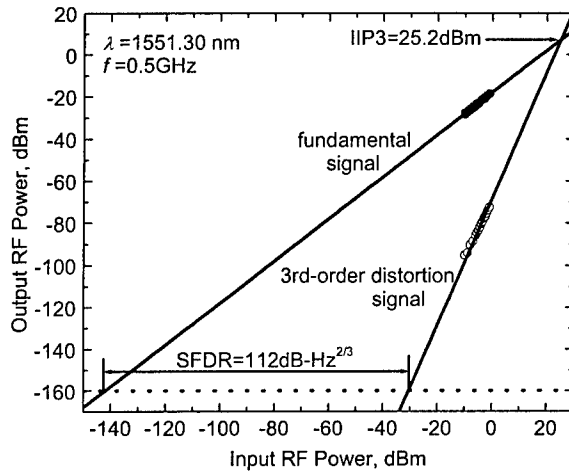

Figure 3.8. Two-tone measurements of the SG-DBR laser with the gain section current of 60 mA.

Conversion efficiency: The modulation efficiency of a directly modulated laser is given by the current conversion efficiency, η_d, and optical coupling losses. For a standard semiconductor laser, the maximum possible conversion efficiency is about 0.8 W/A at 1550nm, also referred to as 100% differential quantum efficiency (DQE). Using a typical 50Ω terminated driver source, a serial matching load is often applied to the laser to minimize reflections. The matching load comes with a price. For a fixed output power from the source, the delivered modulation current to the laser will be nearly half to what is delivered to an unmatched laser, assuming the laser has a low input impedance. Several possibilities exist to enhance the direct modulation response beyond the limit given by
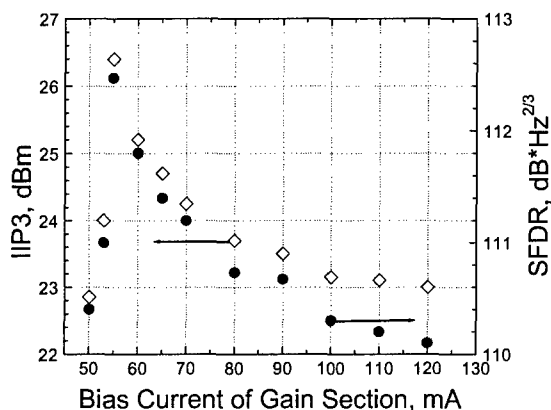
Figure 3.9. SFDR and IIP3 values versus the bias current of the gain section of the SG-DBR. The other three sections were disconnected.

100% DQE. The integrated semiconductor amplifier in the integrated SGDBR-SOA-EAM device provides gain to the modulated signal. The direct modulation efficiency is also conveniently measured by measuring the absorbed photocurrent in the EAM reversed biased for high extinction. In this manner, the direct modulation conversion efficiency can be estimated decoupled from optical coupling losses, even for a fiber-pigtailed packaged device. Figure 3.10 shows the detected EAM photocurrent as a function of gain section bias current, the SOA being biased at a constant 180mA. The maximum slope is of the order of 3.7 in the 30-35 mA range, indicating an equivalent DQE equal to or exceeding 370%, depending on the EAM photodetection responsivity. The higher than unity gain is attributed to the optical gain provided by the SOA. Optical amplification will improve the transmitter gain but also increase the transmitter noise to a higher degree than the slope sensitivity and can therefore only degrade the link noise figure, assuming it is not limited by receiver noise. Also shown in Figure 3.10 is the RF gain at 1 GHz modulation frequency. Up to 17 dB RF gain is measured between 31 mA and 33 mA, a result from the combination of the SOA gain and the ratio between the low input impedance of the unmatched laser and high output impedance of the EAM.
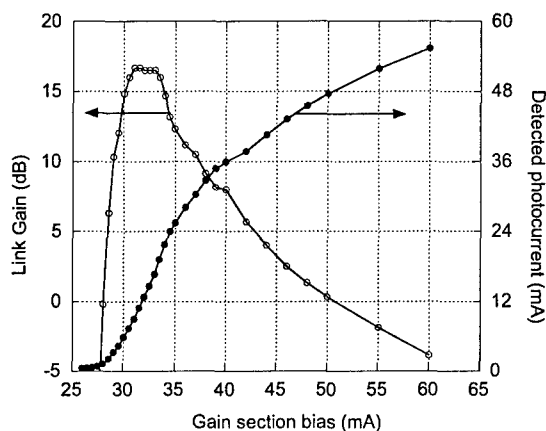

Figure 3.10. Detected photocurrent in the reversed biased EAM as a function of gain section bias. Also shown is the 'on chip' optical link gain at 1 GHz modulation frequency.

34

3.3. Direct modulation: Gain-levered SG-DBR laser

One method of improving the direct modulation sensitivity beyond 100% conversion efficiency without resorting to optical amplification that has been demonstrated is the gain-levered laser. The gain-lever exploits non-uniform pumping of the laser to improve conversion efficiency by biasing one of two sections below threshold, such that the overall laser is biased just above threshold. A prototype gain-levered SG-DBR laser has been produced, dividing the gain section of the laser into two parts, one 500μm and one 100 μm. Enhanced modulation efficiency is obtained pumping the two sections non-uniformly, applying the larger current density to the longer section. Continuous wave room temperature light-lever current measurements were taken as a function of gain section current, and is shown in Figure 3.11. With separately biased gain and lever contacts, I_{th} is reduced and slope efficiency at threshold is increased for increasing I_{Gain}. With shorted gain and lever contacts, threshold current (I_{th}) was 30 mA. At low gain section bias, the gain-lever L-I curve shows a relatively low differential efficiency, similar to that of the gain section. At high gain section current, a stepwise turn-on with hysteretic effect is observed. However, at intermediate gain bias, a rapid turn-on behavior is observed with enhanced differential efficiency. Small signal modulation response was measured on un-terminated devices, Figure 3.12. Although we see hysteretic behavior in the L-I curve, the modulation bandwidth is at least as good as a conventional laser produced by shorting the contacts, 5.0 GHz for I_{gain} = 60 mA and I_{lever} = 8 mA. One limitation of the gain-levered laser approach is that when high differential efficiency is observed, i.e. close to threshold, the bandwidth is generally low.
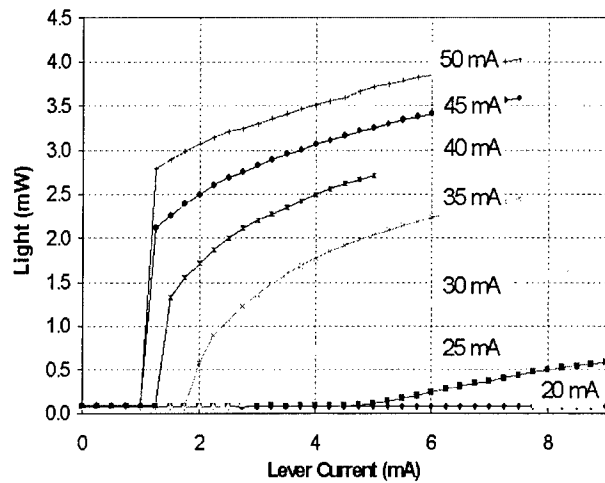

Figure 3.11. DC optical power vs. lever current with gain current as a parameter for I_{SOA} = 30 mA.
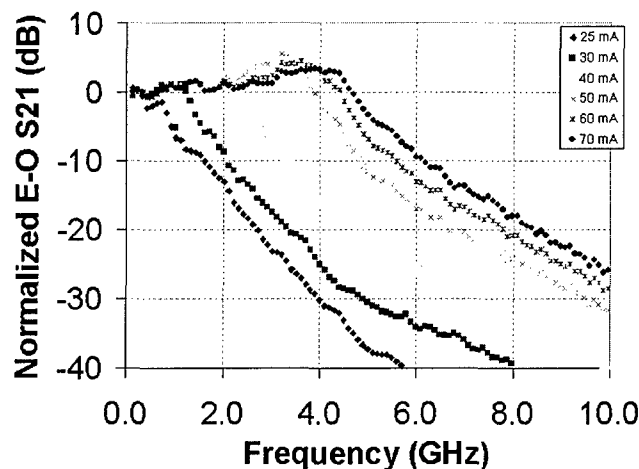
35

Figure 3.12. Small signal gain lever laser bandwidth for different gain section bias points.

3.4. Direct modulation: Bipolar-Cascade Laser

The segmented laser approach does not inherently limit the performance of the analog link beyond that what is achieved using a standard laser. In this biasing scheme, several laser gain section are biased in series, reusing the injection current to achieve more than 100% DQE, as shown in Figure 3.13. The segmented laser improves differential efficiency, threshold current, and matching, it also operates with good CW power, modulates efficiently, at high speed, and with low noise and distortion. In most cases, these comparisons are made with the single stage control laser fabricated alongside the multistage. While these control lasers may not be state of the art themselves, they serve to measure whether the segmentation and cascading of the multistage lasers deteriorates their performance. The dramatic CW results are shown in Figure 3.14, and tabulated in Table 3.1, both for a Fabry-Perot laser. The differential efficiency scales slightly
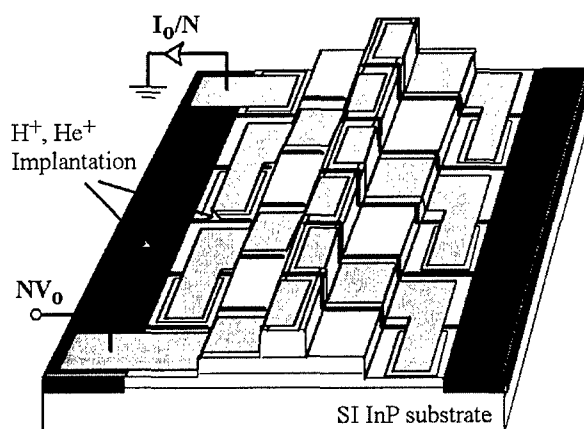

Figure 3.13. 3-d schematic of bipolar cascade segmented ridge laser. The dark grey areas are ion-implated to force current, in series, through N diode stages.

36

sublinearly with the number of stages, increasing steadily to 390% at 12 stages, an 11-fold improvement over the control laser. Threshold current falls as the number of stages increase, with the 12-stage threshold reduced by more than a factor of ten, to 2.74mA. All of the lasers are quite robust, and emit up to 20mW per facet, with a multimode spectrum centered at 1.55μm.
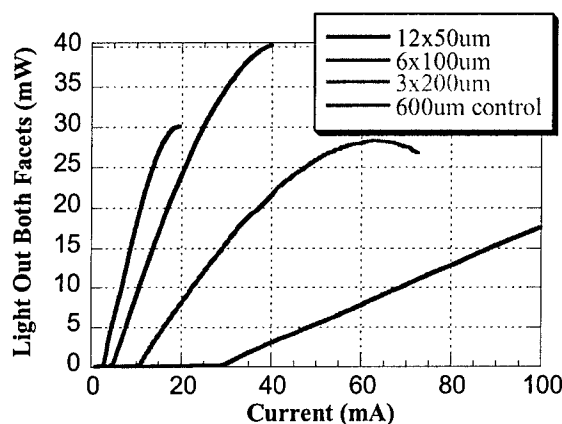

Figure 3.14. L-I response of a 600μm F-P laser, subdivided into 1, 3, 6, and 12 stages. DQE exceeds 100% in all but the control laser.

Stages & Length	Differential Efficiency	Threshold Current	Threshold Voltage	DC Input Impedance
12x50μm	390%	2.74 mA	11.3 V	471 Ω
6x100μm	218%	4.77 mA	5.8 V	117 Ω
3x200μm	126%	10.4 mA	3.0 V	48 Ω
1x600μm	34%	28mA	1.05 V	5.5 Ω

Table 3.1. Room-temperature, CW characteristics of the control and segmented F-P lasers.

Such improvements must be "paid for," and the voltage increases with the number of stages. However, due to the more uniform current density of shorter stages, the voltage per stage drops from 1.05 V in the control laser to 0.94 V in the 12-stage device, ensuring that the threshold power is roughly constant with the number of stages. Resistance scales roughly quadratically with the number of stages, reaching 50Ω for the 3-stage laser which itself has a differential efficiency greater than unity. In practice, the scaling of cascade lasers is limited by the large voltage and impedance of very long diode chains, as well as the finite length of the isolation region between stages, and its optical absorption. However, scaling of the present generation of devices was limited by the shortest stage length (50μm) included on the mask, so longer lasers with up to 19 stages were tested, and lased CW with over 500% DQE, 2.1mA, 19.0V threshold, and 930Ω input impedance. The input impedance of a laser is equal to the slope dV/dI at the laser's bias point, and changes with bias, so it is critical that the laser be well matched near its bias point. Figure 3.15 confirms the 50Ω RF-matching, of a 3-stage laser, extracted from the electrical S_{11} parameter. The laser reaches 50Ω at 21mA (optimal digital transmission

bias = 20.5mA). Figure 3.16 shows S21-data of the 3-section laser with a bandwidth up to ~5GHz at 30mA bias current. The bandwidth of the 3-stage laser was in fact slightly improved to that of the control laser.
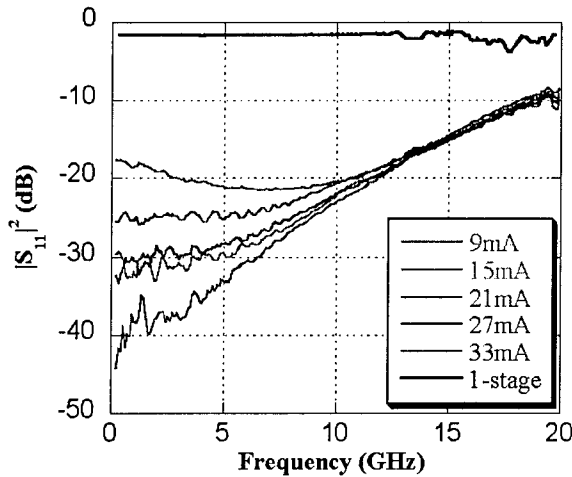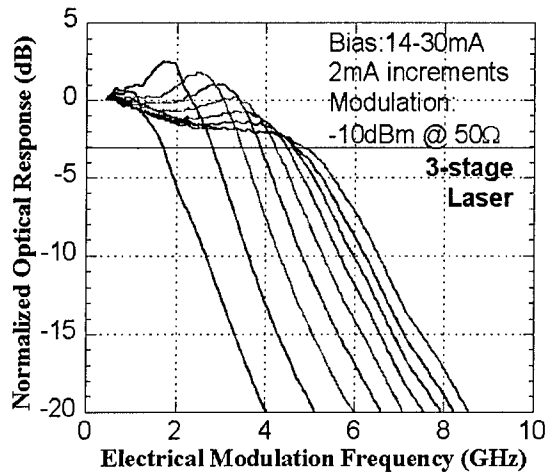

Figure 3.15. 3-stage S11-parameters.

Figure 3.16. 3-stage S11-parameters.

Figure 3.17 shows the SFDR of the three-section laser and the control laser. The measurement is taken at 0.5 GHz with 10MHz frequency offset. Comparable performance is observed between the two lasers confirming that the segmentation does not have any detrimental impact. In fact, the three-stage laser have slightly improved SFDR, mainly due to the slightly higher RIN of the control laser. One underlying reason why the segmented laser would perform better is that because of the segmentation, a more uniform current-distribution is forced throughout the waveguide.
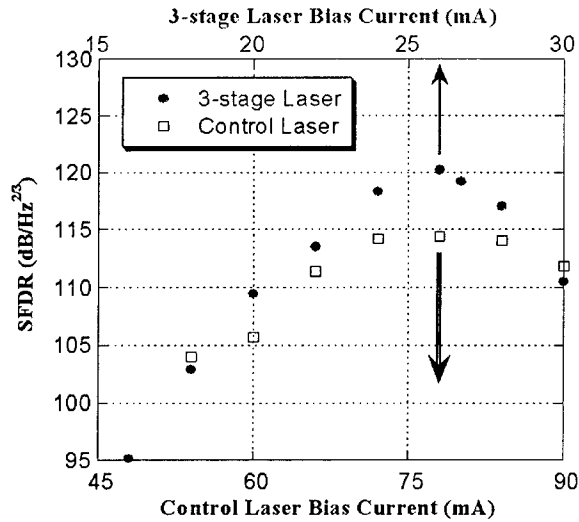
38

Figure 3.17. SFDR for 3-stage and control laser.

Segmented bipolar cascade lasers have also been manufactured in a single longitudinal mode laser structure, and SG-DBR laser. Figure 3.18 shows the segmented gain section devices. Continuous wave room temperature light-current measurements were taken.   The threshold current, single-ended differential efficiency, and input impedance for the 1, 3, 4, and 8 stage devices are 42.5mA, 8%, and 8.5Ω, 15.4mA 22%, and 50Ω, 11.1mA, 26%, and 77Ω, and 7.1mA, 33%, and 222Ω, summarized in Table 4.2. Due to a processing error resulting in poor current injection, these values are not nearly as impressive as they should be, however the threshold current and differential efficiency scales as expected. A segmentation loss of approximately 0.12dB per pass was extracted by plotting the differential efficiency versus the number of stages and fitting to a theoretical curve. The tuning range of 38nm was measured by injecting current into the
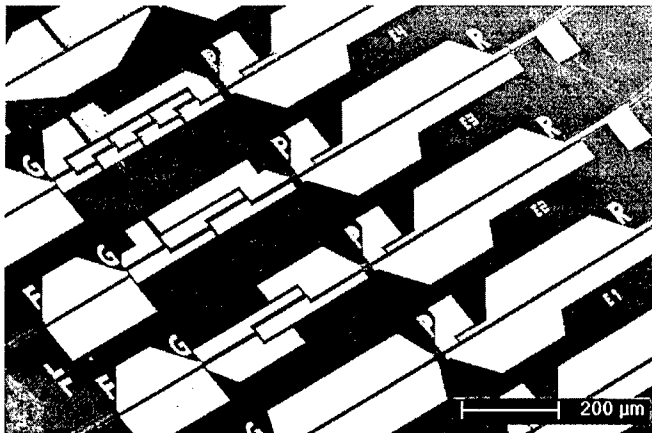

Figure 3.18. SEM of 1-, 3-, 4- and 8-section segmented bipolar-cascade SG-DBR laser

39

front mirror and leaving the rear mirror and phase section unbiased. The optical spectra for various front mirror currents are superimposed in Figure 3.19 showing nearly 40dB side mode suppression ratio without the use of fine tuning of the wavelength. Measurements of the modulation response were performed on un-terminated devices and the results for a 3 stage segmented SGDBR laser are shown in Figure 3.20.

Stages	Ith (mA)	Rslope(Ω)	ηd at DC	ηd 1GHz
1	42.5	9	.1	.087
3	15.4	50	.317	.195
4	11.1	77	.376	.325
8	7.1	234	.5	.446

Table 3.2. Room-temperature, CW characteristics of the control and segmented SG-DBR lasers.
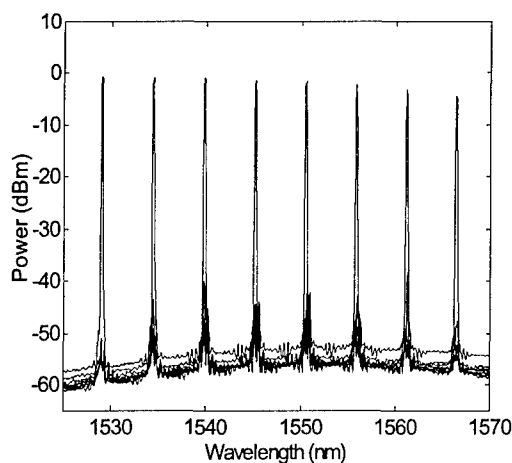

Figure 3.19. Superimposed output spectra over the tuning range of a segmented gain section SGDBR laser.
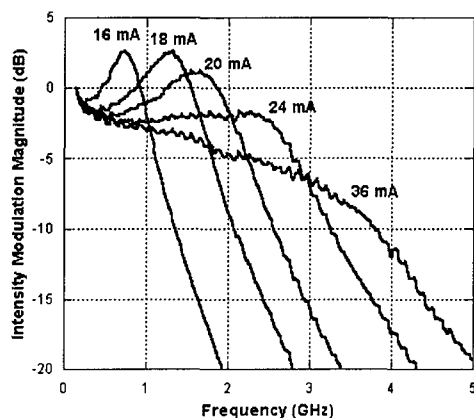

Figure 3.20. Direct modulation bandwidth of the segmented gain section SGDBR laser.

40

3.5. External modulation -EAM

Extensive RF testing have been performed on SG-DBR lasers manufactured by Agility. The integrated electro-absorption modulator used in this work, can be modeled using a simple equivalent circuit, shown in Figure 3.21. R_J and C_J (0.5pF) is the device junction capacitance and resistance, R_S (7Ω) is the device shunt resistance, L_C (0.8nH) is the bondwire inductance and C_P (0.5pF) is the bonding-pad capacitance. The photocurrent can be modeled as an equivalent change in junction resistance. As a result of integration of the source and modulator, and the bulk design of the modulator, high optical power can be coupled to the EAM without risking damage to the device or degrading the extinction of the device. Facet damage limits the available input optical power to waveguide p-i-n photodetectors to typically 200 mW, while quantum-well modulators can be saturated even at moderate optical power due to screening effects. The high operating waveguide power of the device is illustrated by Figure 3.22, where the complementary measurement of transmitted fiber-coupled power and absorbed photocurrent in the modulator is shown for 1552nm. In fact, the photocurrent follows an almost perfectly linear relation to the waveguide optical power to photocurrents higher than 70 mA. Clearly, this configuration enables study of high photocurrent effects in electroabsorption modulators. The maximum slope of the V-I curve in Figure 3.22 corresponds to an equivalent device resistance of 50Ω. This affects the response of the modulator. Figure 3.23 shows S11 of the EAM in the absence of any matching circuit. The input optical power is regulated by adjusting the bias current of the SOA. It is seen that the reflections are strongly dependent on the input optical power and at 115 mA SOA bias, an almost perfect 50Ω match is achieved at lower frequencies. At higher frequencies, the reflections are also determined by the junction and pad capacitances and the bond-wire inductance. The dip in the S11 response above 10 GHz is caused by interaction between the bond-wire inductance and the capacitance at the AlN-substrate the device is mounted on. The equivalent device conductance can be derived from the reflections and plotted as a function of fiber-coupled optical power, shown in Figure 3.24. It is seen that the conductance varies linearly with the optical power and can be as high as 0.029 S, corresponding to only 27Ω junction resistance in series with 7Ω shunt resistance.
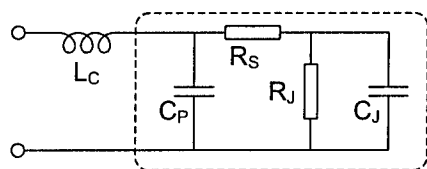

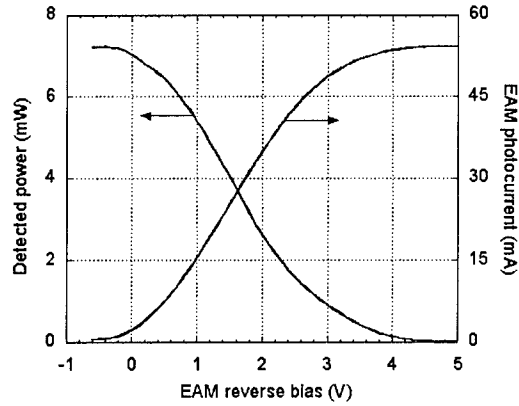*Figure 3.21. EAM RF equivalent circuit model*

Figure 3.22. Fiber-coupled transmitted power and EAM photocurrent as a function of EAM reverse bias at 1552 nm.
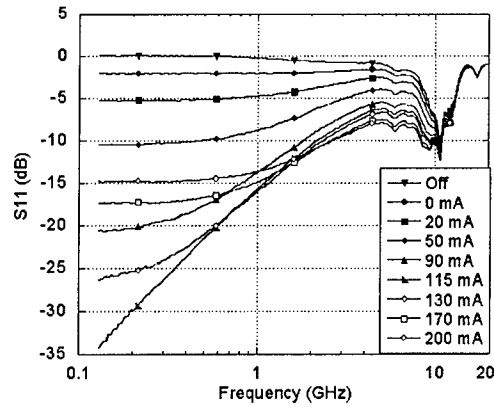

Figure 3.23. EAM S11 as a function SOA bias current with 180 mA gain section current.
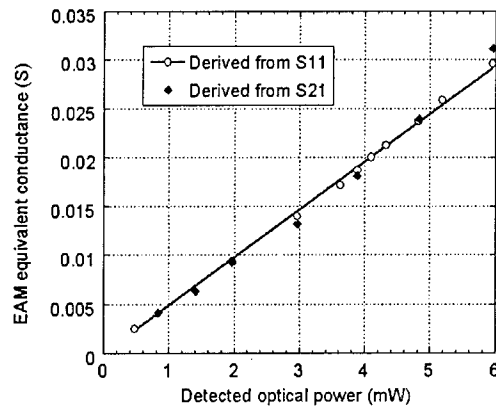

Figure 3.24. Equivalent EAM conductance as a function of fiber-coupled transmitted optical power, derived from S-parameters, as a function of fiber-coupled transmitted power.
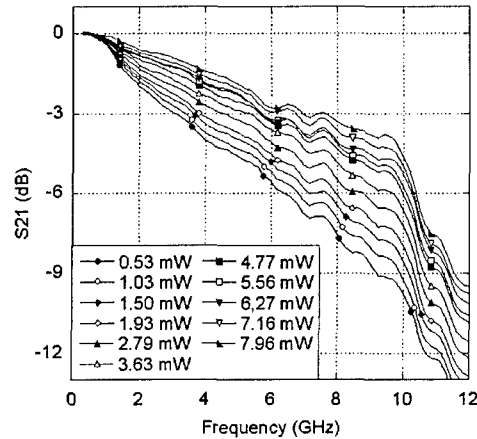
42

Figure 3.25. Measured EAM modulation response for different levels of fiber-coupled transmitted optical power.

Modulation response: The absorbed photocurrent has dramatic effects on the modulation response of the EAM. Normally, an optical modulator is assumed to have a high input impedance, therefore the RF to optical conversion efficiency is determined by the voltage slope efficiency, dP/dv_m, and the parallel matching load, often 50Ω, that is used for matching and providing a high bandwidth. The effects of photocurrent can be investigated by considering the modulator current slope efficiency, dP/di_m. The current slope efficiency is independent on dP/dv_m, only related to the amount of absorbed optical power by the photodetection slope efficiency, η_i, with a maximum value of 1.24A/W at 1550nm, and optical coupling losses. The slope efficiency can not exceed the limit given by η_i, the EAM shunt resistance and the driver output load. The photocurrent will therefore result in a compression of modulation sensitivity at lower frequencies, which in term will affect the bandwidth. Figure 3.25 shows the normalized modulation response at different transmitted optical power levels for an unterminated EAM. The 3-dB modulation bandwidth is shown to increase from 3.3GHz to closer to 8.0 GHz with optical power. Deriving the device conductance from the compression of the S21 measurements, there is good agreement compared to S11 data, also shown in Figure 3.23. The EAM is currently not optimized for high bandwidth, for a 50Ω terminated EAM, the bandwidth is about 6.5 GHz at low optical power, limited by pad and junction capacitance of about 0.5pF each. A substantial improvement in modulator bandwidth can be obtained by minimizing pad capacitance. By reducing the EAM modulator length from 250μm to 120μm, the bandwidth increases to about 9 GHz at the price of lower modulation sensitivity.
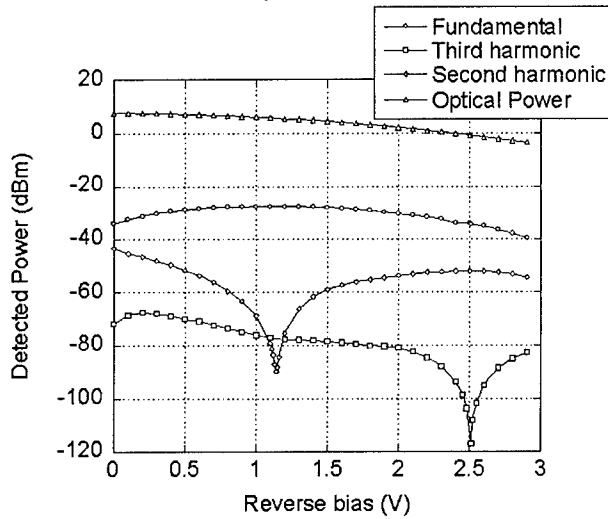
43

Figure 3.26. Detected Optical power and RF power of fundamental and distortion products for 0 dBm modulation power.

Dynamic range: The spurious-free dynamic range (SFDR) of the device is measured using two-tone modulation at 1 MHz offset of between -5 dBm to 8 dBm modulation power each. Figure 3.26 shows the power of the fundamental, second and third harmonic intermodulation products as a function of EAM bias for 0 dBm modulation power of each carrier and at 0.5 GHz. Also shown in the plot is the optical output power, all for 100 mA bias current to gain and SOA sections at 1545 nm wavelength. Minimum second order distortion is observed at the bias point where the modulation efficiency is maximum, -1.1 V at 1545 nm. Minimum third order distortion appears at -2.5 V EAM bias voltage.

For broadband linearized applications, both even order and odd order distortion products need to be taken into consideration. The optimum bias point for broadband operation is therefore at maximum slope efficiency, minimizing second order distortion. Figure 3.27 shows the measured dynamic range, both for 1Hz and 1MHz bandwidth, limited by second or third order intermodulation products for 180 mA bias to SOA and gain sections and 1552 nm. The received optical power is 6.3mW, resulting in a noise floor at −157 dBm/Hz, limited by shot noise and laser RIN. Due to the different slope dependence of second and third order distortion, the SFDR is limited by third order distortion measured in noise bandwidths down to about 200 kHz, after which second order distortion will be limiting. The SFDR limited by second order distortion is 97.19 dB in 1 Hz bandwidth, corresponding to 67.19 dB in 1 MHz bandwidth. The SFDR limited by third order distortion is 106.09 dB in 1 Hz bandwidth, corresponding to 66.09 dB in 1 MHz bandwidth. Figure 3.29 shows the broadband SFDR over the tuning range of the laser. The SFDR remains within a 103-107 dB/Hz$^{2/3}$ range limited by third order intermodulation products, or 95-98 dB/Hz$^{1/2}$ range limited by second order intermodulation products.

44

Figure 3.27. Measured power of noise floor, fundamental, second and third order intermodulation products at 1552 nm, for –5 dBm to 5 dBm input RF power, 6.3mW optical power and –1.1V EAM bias. Broadband spurious-free dynamic range is also shown in 1Hz and 1MHz bandwidth.

For sub-octave linearized applications, even order distortion products can be filtered away after detection. The EAM is therefore low biased to the bias point of minimum third order distortion, resulting in a fifth order slope dependence of the distortion at detectable power. Figure 3.28 shows the measured sub-octave dynamic range, both for 1Hz and 1MHz bandwidth. The SFDR is limited by fifth order intermodulation products for 120 mA bias to the SOA and 180 mA to the gain section and 1552 nm. The lower bias applied to the SOA is to protect the modulator from Joule-heating by excessive i–v product, i being the EAM photocurrent. The received optical power is 0.96mW, resulting in a noise floor mainly limited by shot noise. The SFDR is 126.28 dB in 1 Hz bandwidth,
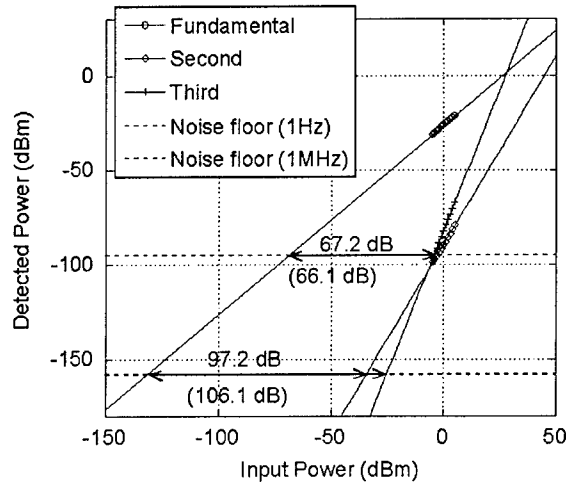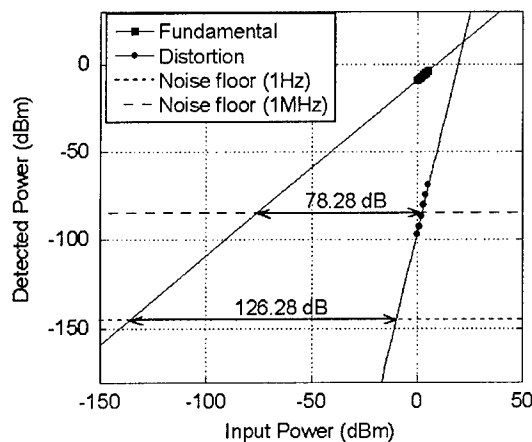

Figure 3.28. Measured power of noise floor, fundamental, second and third order intermodulation products at 1552 nm, for 0 dBm to 5 dBm input RF power, 0.96mW optical power and –2.5V EAM bias. Sub-octave spurious-free dynamic range is also shown in 1Hz and 1MHz bandwidth.

45

corresponding to 78.28 dB in 1 MHz bandwidth. For comparison, the same performance in 1 MHz bandwidth would be offered by a SFDR of 118 dB in 1 Hz for a device limited by third order distortion products, an important consideration when comparing, say, the performance of external modulators biased for minimum third order distortion to that of directly modulated lasers. Figure 3.29 shows the sub-octave SFDR over the tuning range of the laser. The SFDR remains within a 125-127 dB/Hz$^{4/5}$ range, all limited by fifth order intermodulation products.
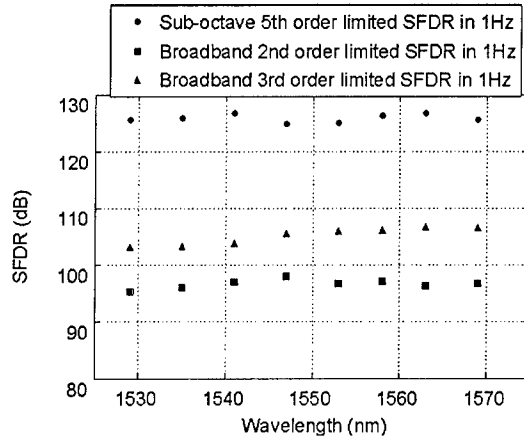

Figure 3.29. Measured sub-octave and broadband spurious-free dynamic rage, left scale, normalized to 1 Hz bandwidth for different wavelengths. Sub-octave SFDR limited by fifth order intermodulation products and broadband SFDR limited by second and third order intermodulation products.

The power of the distortion products relative to the fundamental and optimum EAM bias point for minimum distortion do not change significantly for modulation frequencies within the bandwidth of the modulator, up to 10 GHz for a 50Ω terminated device. This is shown in Figure 3.30 where the measured SFDR is plotted as a function of modulation frequency over a range of 0.5 GHz to 10 GHz, both for 1 MHz noise bandwidth and normalized to 1 Hz. A 120μm long device was here used to provide sufficient bandwidth. Also inset in the figure is the combined effect of RIN and shot noise of the laser. It is seen that the frequency-dependent variation of the measured SFDR can be explained down to less than 2 dB margin by the RIN level, indicating relatively frequency independent linearity behavior of the EAM. Improved SFDR can therefore be achieved by reducing the RIN level at higher frequencies by increasing gain section bias, as indicated by Figure 3.2. However, to do this, the power handling of the device will need to be improved to accommodate the increased Joule-heating. At all frequencies, the third order distortion products could be suppressed to a level such that the sub-harmonic SFDR was limited by fifth order distortion products. The EAM bias point needed to achieve this varied in a -2.95+/-0.1V range. The cause for this variation of bias point was residual distortion from the RF sources, even though care was taken to reduce the residual relative distortion to a level suppressed by at least 15dB to that of the modulator. The magnitude of the distortion of the EAM was insensitive to the residual distortion of the RF sources.
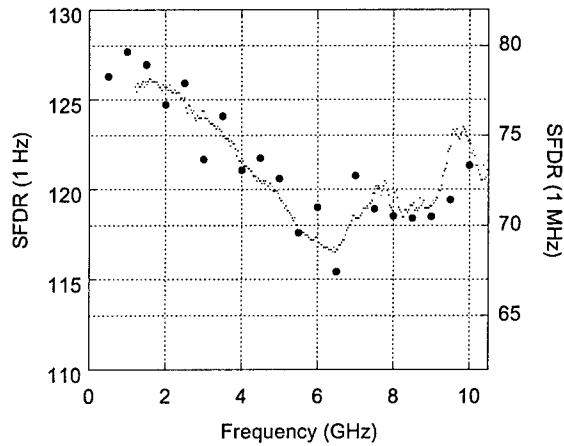
Figure 3.30. Measured EAM SFDR versus modulation frequency for 1 MHz bandwidth and normalized to 1 Hz at 1554 nm. Also inset is relative effect on SFDR from the RIN level of the source.

The integrated SGDBR-SOA-EAM device was applied as the optical transmitter in an analog link experiment. Microwave to optical conversion was achieved by modulating an unmatched EAM, while a 50Ω back-terminated 0.8A/W Discovery photodetector was used for optical to microwave conversion. Figure 3.31 shows the resulting link gain and noise figure as a function of EAM bias at 1552nm and 1GHz modulation frequency. The link gain peaks at –20.7dB between –1.4V and –1.5V EAM bias voltage. The gain can be improved towards overall conversion gain by removing the back-termination of the detector, improving the gain by 6 dB gain, the optical coupling could be potentially be improved by 3-5 dB optical (= 6-10 dB electrical), and using a high impedance receiver circuit. Reducing the transmitter fiber coupling loss will improve the gain further.
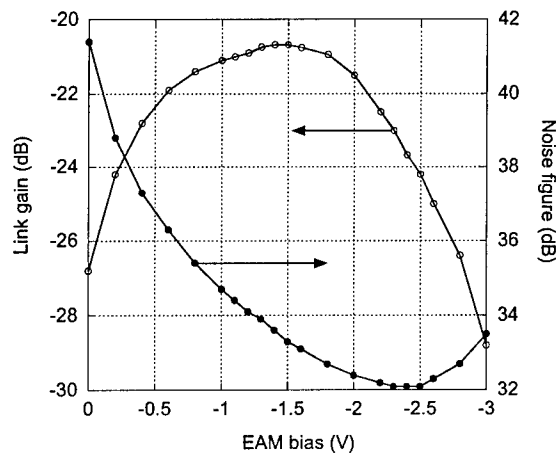

Figure 3.31. Link gain and noise figure as a function of EAM bias voltage at 1552 nm for 180 mA gain section bias and 120 mA SOA bias.

47

However, ultimately to achieve sufficient optical link gain to achieve low noise figure, the limitations imposed by the EAM photocurrent need to be addressed. Using the limit derived for maximum conversion efficiency of an EAM, derived in the last section, increasing the optical power will only improve the link gain by a maximum 4.6 dB, limiting the available gain of the link in the current configuration to −16.1 dB, as illustrated by Figure 3.32.
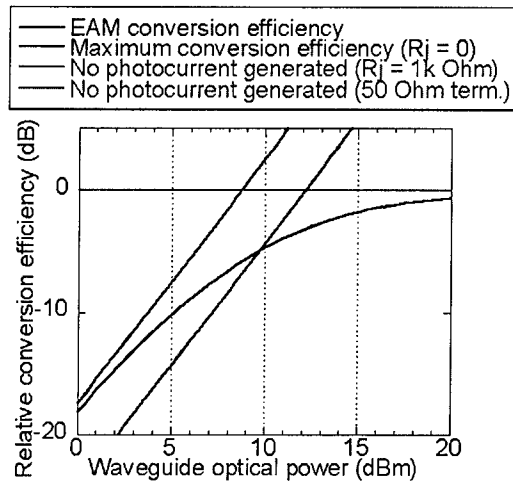

Figure 3.32. Link gain not including photocurrent-effects and real link gain relative to maximum potential link gain as determined by EA photocurrent.

The link noise figure reaches its lowest level at a voltage different from where the link gain peaks. The reason for this is found in the RIN limited noise characteristic of the link. While the decreasing average output optical power at lower EAM bias will not change the level of the noise floor relative to optical power, the relative slope sensitivity will increase and so will then the modulated signal level, normalized by average transmitted power. There exists an optimum EAM bias for minimum noise figure where the improvements in relative slope sensitivity and the onset of shot noise limited noise performance balances out, here −2.4V resulting in 32.1dB NF. This phenomenon has been referred to as 'low biasing' the external modulator and has been observed using well-balanced Mach-Zehnder modulators. Figure 3.33 shows the link gain and noise figure as a function of applied SOA bias, again at 1552 nm and 1GHz modulation frequency, the EAM being biased at maximum slope sensitivity. As expected, the link gain increases with SOA bias and optical power. The noise figure, however, reaches a minimum level between 100mA to 120mA. Compared to the measured RIN performance versus SOA bias, shown in Figure 3.33, the best noise performance is slightly shifted to lower values of SOA bias current. This can be attributed to additional heating of the device from the absorbed EAM photocurrent.
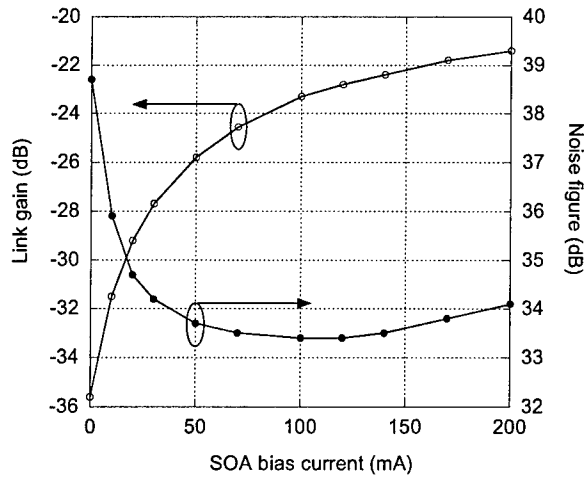
48

Figure 3.33. Link gain and noise figure as a function of SOA bias current at 1552 nm for 180 mA gain section bias and –1.4V EAM bias.

3.6. External modulation -Tandem EAM

The combination of multiple modulators allows for modification of the nonlinear response of two modulators to cancel out the nonlinearity of the total response. Split contact Dual EAM structures for improved linearity as shown in Figure 3.34 have been explored for this purpose. A split contact dual EAM structure allows for a greater number of parameters to be changed, influencing the overall response of the modulator; such as using different bias points to each section and changing the splitting ratio of the modulation applied to the two sections. The total absorption will be the product of the absorption of the two sections. Because of the exponential-like response of a pure Franz-
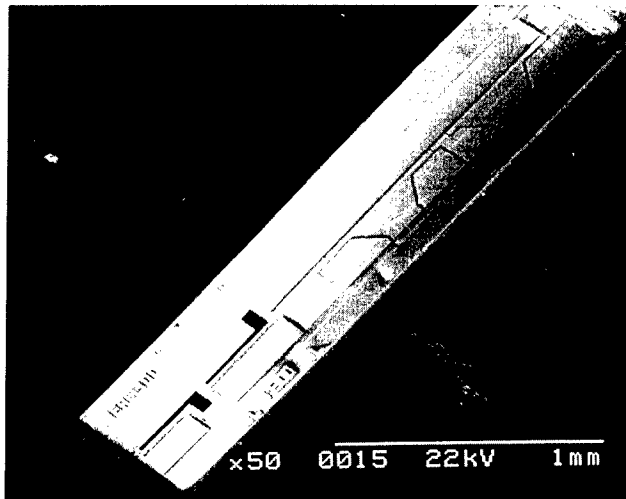

Figure 3.34.   Device SEM with Dual 300um EAM devices integrated with SGDBR

49

Keldysh modulator, the product of the response of two sections will display a similar pattern of second and third order nulls as the response of a single section device. However, the split contact approach will offer increased flexibility to obtain improved performance from modulators with altered response, such as QCSE or combined FKE/QCSE tuned modulators, particularly if these devices have initially been optimized for linear operation.

Most previously investigated tunable transmitters use an offset quantum-well structure, where passive sections are defined by selectable etching of the quantum-well material. Using this process, the electroabsorption modulator is limited to bulk material, Franz-Keldysh effect (FKE) type modulators only. Even though FKE modulators are well-suited for integration with widely tunable lasers due to wide spectral bandwidth, the robust, but relatively inflexible absorption characteristics of FKE modulators gives little room for tailoring a material that can be used for a modulator with a more linear absorption response.

One approach to overcome some of the limitations of FKE modulators, in terms of linearity is to use quantum-confined Stark-effect (QCSE) modulators. This can be realized for integrated devices using quantum-well intermixing (QWI) techniques. We have developed a QWI technology well suited for integrated photonic devices based around a widely tunable SGDBR laser, that allows for inclusion of electroabsorption modulators with tailorable bandgap. A tandem EAM with each a different bandgap and integrated with an SGDBR laser has been produced. The tandem modulators were 175μm long each and were intermixed to a bandgap of 1465nm and 1495nm respectively. The non-intermixed quantum-well material of the laser emitted around 1550nm. Figure 3.35 shows measured absorption curves for the two modulator sections for different emitted wavelengths from the SGDBR laser. It is expected that by taking advantage of this technology, either a tandem modulator with selected dual bandgap, or a single modulator with a tailored graded bandgap will produce modulators with a linearized response.
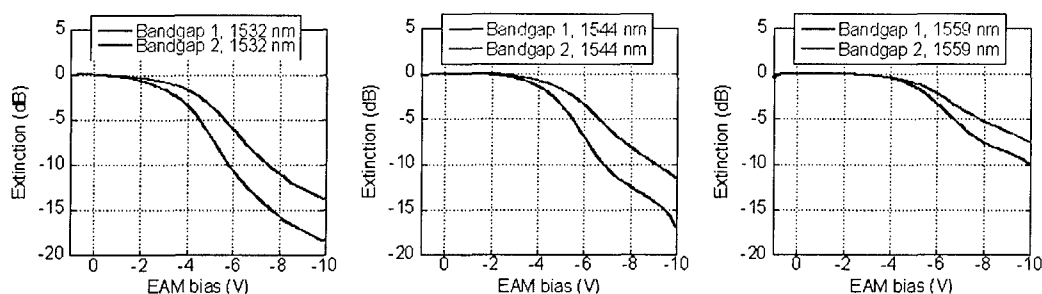

Figure 3.35. Measured extinction curves for different bandgap modulators at 1532,1544 and 1559nm wavelength. Bandgap 1 is at 1465nm and bandgap 2 is at 1495nm.

The 3-dB bandwidth of intermixed QCSE modulator is 19 GHz, as shown in Figure 3.36. The improved bandwidth of the device has been achieved by selectively implant areas outside the central buried waveguide and the intermixed wells to reduce overall capacitance.
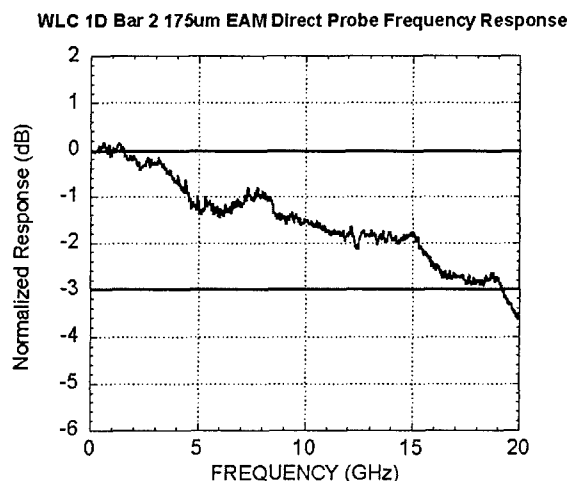
WLC 1D Bar 2 175um EAM Direct Probe Frequency Response

Figure 3.36. Measured frequency response for 175 μm QWI QCSE EAM.

3.7. External modulation -MZM

A Mach-Zehnder modulator can overcome some of the limitations that an EAM has, in particular saturation effects due to absorbed photocurrent. MZ-modulators integrated with MZ modulators have been pioneered at UCSB. The device used for this work consists of Mach-Zehnder modulator, a widely-tunable sampled-grating (SG) DBR laser and an SOA, all integrated on a single InP chip. The chip is mounted on an Aluminum Nitride ceramic carrier with coplanar RF lines connecting the MZ electrodes. A schematic of the device structure is shown in Figure 3.37. Also inset in Figure 3.37 is a detail of the MZ modulator, incorporating 300 μm long RF electrodes on each arm, allowing single or dual drive.
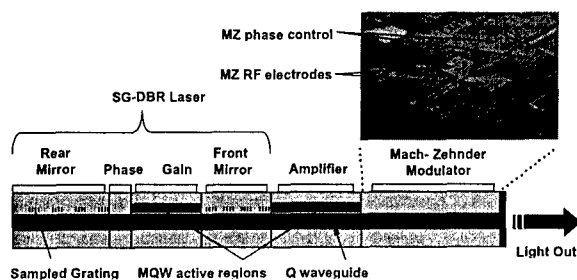

Figure 3.37. Simple schematic of the integrated device including a detail picture of the MZ modulator.
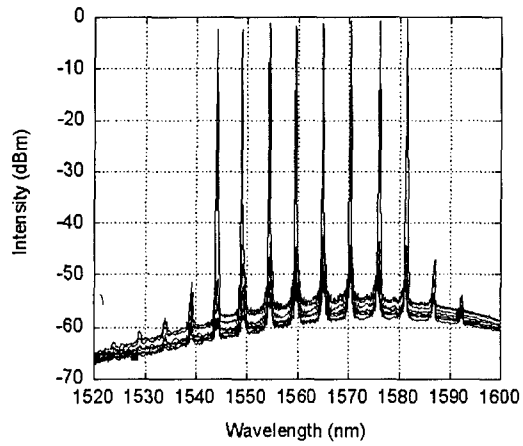
51

Figure 3.38. Overlapped optical spectra taken over the tuning range of the SG-DBR laser.
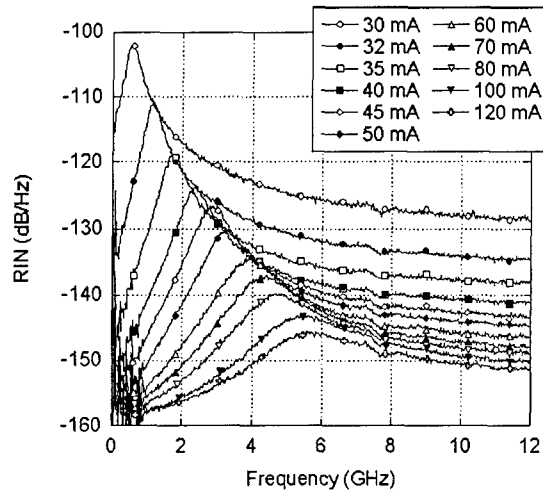

Figure 3.39. Measured RIN at 1555 nm for different gain section bias and 100 mA SOA bias current.
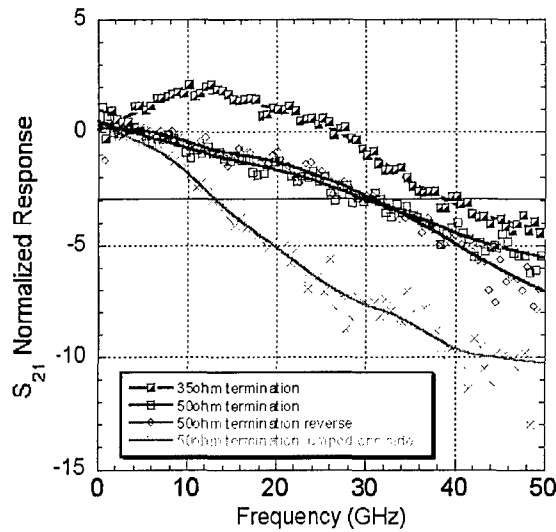
Figure 3.40. Mach-Zehnder frequency response taken at 1555 nm and at –3V bias.

The SG-DBR laser has over 38 nm wavelength tuning range, from 1544 nm to 1482 nm with more than 40 dB sidemode suppression ratio and a fiber-coupled output power better than 2mW over the tuning range. Figure 3.38 shows the overlapped optical spectra taken over the tuning range of the SG-DBR laser, varying the front mirror current only. The relative intensity noise has been measured and is shown in Figure 3.39 for a wavelength of 1555 nm. The SOA current was kept fixed at 100 mA, while the gain section current was varied. At 120 mA gain section current, the RIN was lower than –146 dB/Hz. The 3-dB bandwidth of a lumped MZ modulator is 12.4 GHz. However, the bandwidth can be improved by driving the two electrodes of the MZ in series-push-pull configuration. This distributes the applied modulation voltage equally between the electrodes, resulting in half the voltage per electrode, but the same total MZ phase shift and unchanged V-pi. By series-connecting two diodes, the capacitance is halved, resulting in a dramatically improved frequency response, as shown in Figure 3.40 for 300 µm long RF electrodes. Additionally, in series-connected configuration, the RF impedance of the modulator is increased, resulting in an all-together more than doubling of the bandwidth relative to lumped performance. With 50 Ohm termination, the 3-dB bandwidth is measured at 30 GHz, and reducing the load to 35 Ohm, 40 GHz is measured.

When applying the modulation voltage to the electrodes of a Mach-Zehnder, both amplitude and phase are modulated, resulting in a modulator response slightly different than the conventional sinusoidal response of a MZ modulator. This is illustrated in Figure 3.41, where the measured transmitted optical power of the device is mapped out as a function MZ electrode biases. It can be seen that for equal voltage to the arms of the MZ, the amplitude of the arms is balanced and high extinction is achieved, while for unequal applied voltage, a high extinction cannot be obtained even though the output of the two arms is in antiphase. This is because the absorption in the arms at lower applied bias creates an amplitude imbalance.
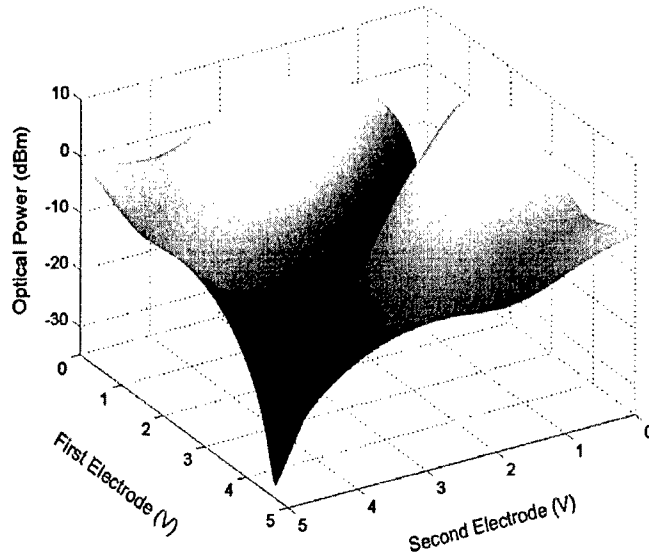
Figure 3.41. Measured transmitted optical power of the device as a function MZ electrode biases.

The slightly modified MZ response creates an opportunity for linear operation. Different from the purely sinusoidal response of the conventional MZ modulator, the minimum of the power the third harmonic intermodulation products does not appear at the same bias as for the minimum of the fundamental as shown by Figure 3.42, where the detected RF power of fundamental and intermodulation products are plotted together with the transmitted optical power.

Figure 3.42. Detected average optical power and RF power of fundamental and intermodulation products for 0 dBm modulation power.

54

Figure 3.43. Measured power of noise floor, fundamental, second and third order intermodulation products at 1555 nm at –1V MZ bias. Intermodulation products are measured at different carrier separation. Sub-octave spurious-free dynamic range is shown in 1Hz and 1MHz bandwidth.

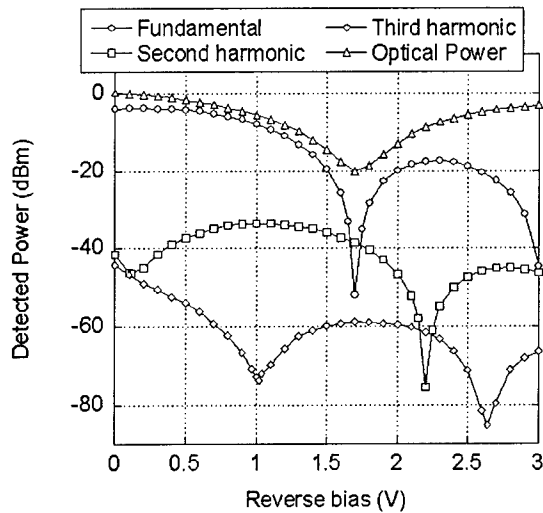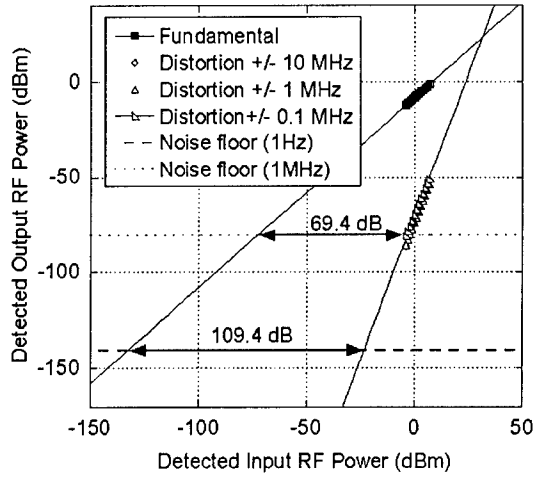The bias point for sub-octave linear operation is –1V. This is a compromise between maximizing the output power of both MZ arms in order to achieve high slope sensitivity, and the requirement for some intensity modulation in the MZ electrode to achieve the modified MZ response described above. The MZ phase is then adjusted to the point of minimum third order distortion, as shown in Figure 3.42. For broadband operation, both second and third order intermodulation products need to be considered. The optimum bias point is then at minimum second order distortion and maximum slope; –0.1V.

Figure 3.43 shows the sub-octave SFDR at 1555 nm. The SFDR is determined around 0.5 GHz modulation frequency using two-tone modulation for a range of frequency separations between the tones. The SFDR is 109.4 dB·Hz$^{2/3}$, determined from the tone separation displaying the worst nonlinear behavior. Compared to the bias point of maximum slope; –0.1V, shifting the bias to minimum third order distortion, –1V, results in 27dB suppression of third order intermodulation products with only 4 dB modulator gain penalty.
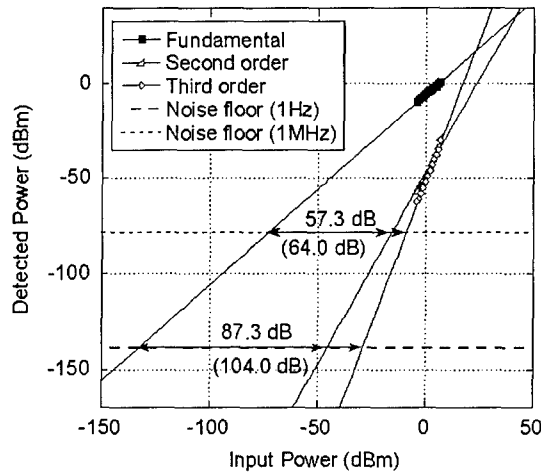
Figure 3.44. Measured power of noise floor, fundamental, second and third order intermodulation products at 1555 nm and −0.1V MZ bias. Broadband spurious-free dynamic range is shown in 1Hz and 1MHz bandwidth.

Figure 3.44 shows the broadband SFDR; 87.3 dB·Hz$^{1/2}$ limited by second order intermodulation products, or 104.0 dB·Hz$^{2/3}$ limited by third order intermodulation products. Similar performance is obtained throughout the tuning range of the laser. As shown in Figure 3.45, the sub-octave SFDR varies between 106.6 dB·Hz$^{2/3}$ to 111.2 dB·Hz$^{2/3}$ and the broadband over 85.7 dB·Hz$^{1/2}$ to 87.9 dB·Hz$^{1/2}$, limited by second order intermodulation products, or 102.0 dB·Hz$^{2/3}$ to 104.3 dB·Hz$^{2/3}$, limited by third order intermodulation products.
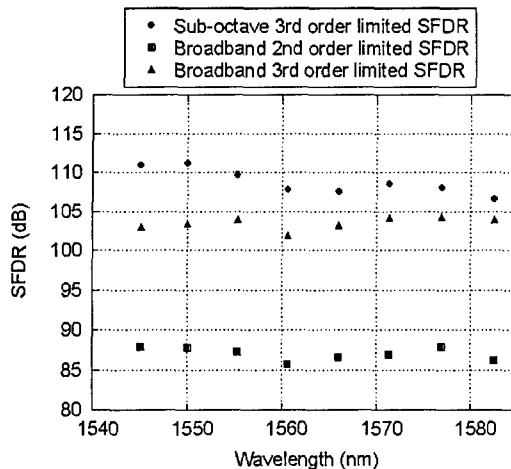
Figure 3.45. Measured sub-octave and broadband spurious-free dynamic range, left scale, normalized to 1 Hz bandwidth for different wavelengths. Sub-octave SFDR limited by third order intermodulation products and broadband SFDR limited by second and third order intermodulation products are shown.

56

In addition to characterization of SGDBR-SOA-MZM devices manufactured at UCSB, similar devices produced at Agility have been characterized. The performance was comparable to that of the UCSB devices. Sample performance can be seen in Figure 3.46 where a 10 GHz 3-dB bandwidth of a 400-μm device is shown. Figure 3.47 shows a typical broadband SFDR performance, biased at minimum second order intermodulation products.
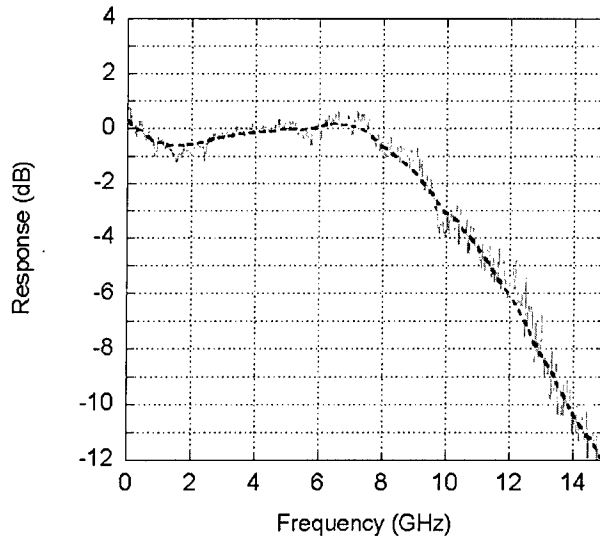
Figure 3.46. Measured bandwidth of a 400μm MZ device produced by Agility.
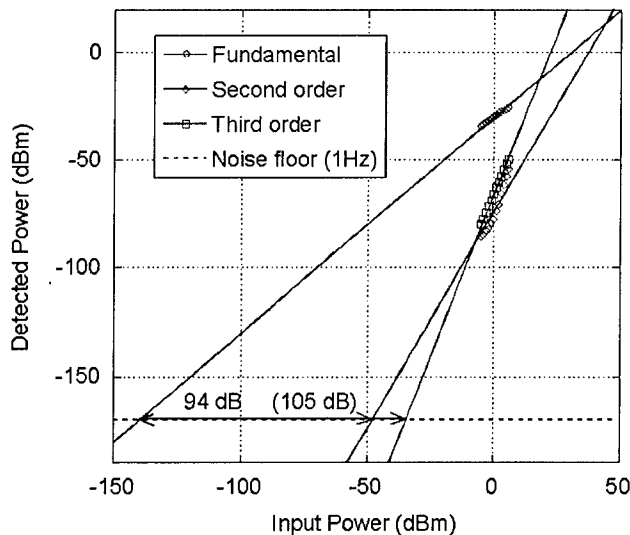
Figure 3.47. Broadband SFDR performance of a 400μm MZ device produced by Agility.

57

4. Traveling-Wave Amplification Photodetectors

4.1 Introduction

High speed, high efficiency and high saturation power are desired characteristics for photodetectors in RF fiber-optic links. Traveling-wave amplification photodetectors (TAP detectors) are designed with the intent to meet all these requirements. TAP detectors combine amplification and absorption regions in a distributed fashion and therefore have potential of achieving record efficiency. There are three approaches to making TAP detectors, as shown in Figure 4.1. One approach is to sequentially combine absorption and gain regions (Figure 4.1.a). The segments are designed such that the peak local photocurrent remains below saturation levels. Alternatively, gain and absorption can occur simultaneously as the mode travels down the waveguide. The gain and absorption regions can be arranged laterally (Figure 4.1.b) or vertically (Figure 4.1.c). The advantages and disadvantages of these three designs are as follows.

Sequential TAP detector: The sequential design may be impedance and velocity-matched, resulting in excellent microwave propagation properties and hence high potential bandwidth (>100 GHz). The absence of a parasitic transistor (described in detail below), together with the minimal angle of spontaneous emission coupled into the absorption region minimizes the background current. The main drawback of this design is the difficult fabrication

Parallel TAP detectors (lateral or vertical): The two parallel designs are very similar. Both the lateral and the vertical configuration have loss-limited high-speed performance. Both configurations are very sensitive to the design of the waveguides. Having too much of the optical energy travel down the amplification region results in saturation, while the opposite leads to limited efficiency. The lateral design is similar to the sequential design in that there is no parasitic transistor and that the coupling of spontaneous emission into the absorption region is small, thereby limiting the background current. However, just like for the sequential design, the fabrication is difficult. The main advantages of the vertical TAP detector are easy fabrication and the possibility of optimizing the active regions for gain and absorption individually, while still be able to grow the structure in one epitaxial growth. The disadvantages of the vertical design are the parasitic transistor effect, which can be minimized by bandgap engineering, and the large coupling of spontaneous emission from the amplification region into the detector region, which results in increased background current.

The objective of this project was to demonstrate the first TAP detectors, analyze this new class of devices, and develop a theoretical model that describes the behavior of these devices. To achieve this, ease of fabrication was determined to be very important, and therefore the vertically coupled design was chosen. Devices were fabricated in GaAs for 850-nm wavelength, and in InP for 1.55-μm wavelength. Over 200% efficiency was achieved for the GaAs devices and over 100% efficiency was achieved for the InP devices. This reports starts with a qualitative discussion of the importance of different modes and guiding in vertical TAP detectors, followed by an analysis of the background current and it's different components. The design and fabrication of vertical TAP detectors are described in the following sections, and experimental results are presented and analyzed. Finally, the sequential TAP detector design is analyzed theoretically.
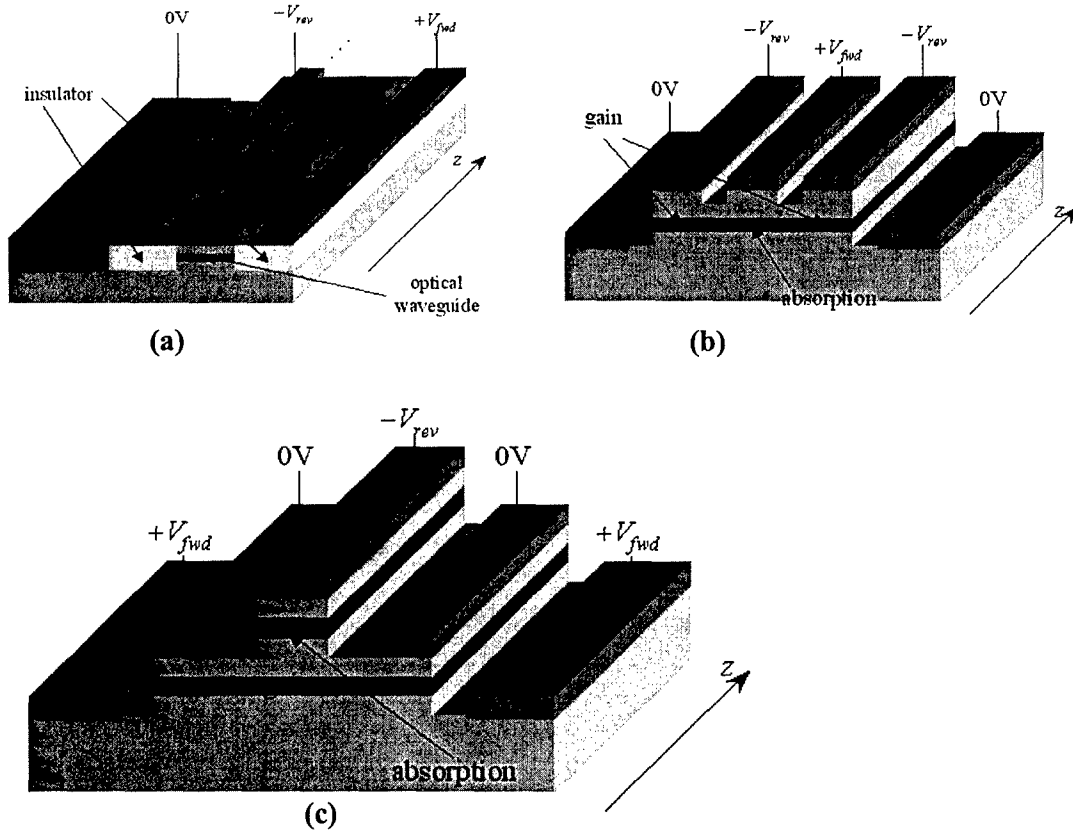
Figure 4.1. TAP detector designs: sequential (a), lateral (b), vertical (c).

4.2 Modes and Guiding in Vertical TAP Detectors

The EO response of TAP detectors is given by the superposition of the photocurrents generated by three types of modes, exhibiting different behaviors. We denote these three types of modes as "detector modes," "amplifier modes," and "cladding modes," as shown in Figure 4.2. Detector modes have large overlap with the absorption region. They are short lived, propagating over short length (~10-50 μm) before being fully absorbed. They are not heavily influenced by the gain in the amplification region, and their response does not significantly depend on the bias current applied between bottom and middle claddings (bias current injected into the gain diode). They are responsible for generating most of the photocurrent detected when the gain diode is left unbiased. Amplifier modes exhibit a large overlap with the gain region and a smaller overlap with the detection region. These modes may actually reach a zero net gain, through the joint action of amplification, absorption, and loss. This "zero modal gain" situation is, in fact, the most interesting operating point for TAP detectors. The amplifier modes are responsible for most of the photocurrent increase as a higher bias current is injected into the gain diode, thus enabling a higher than 100% external quantum efficiency. Cladding modes reside mostly in the bottom cladding, overlapping partially with the gain region,
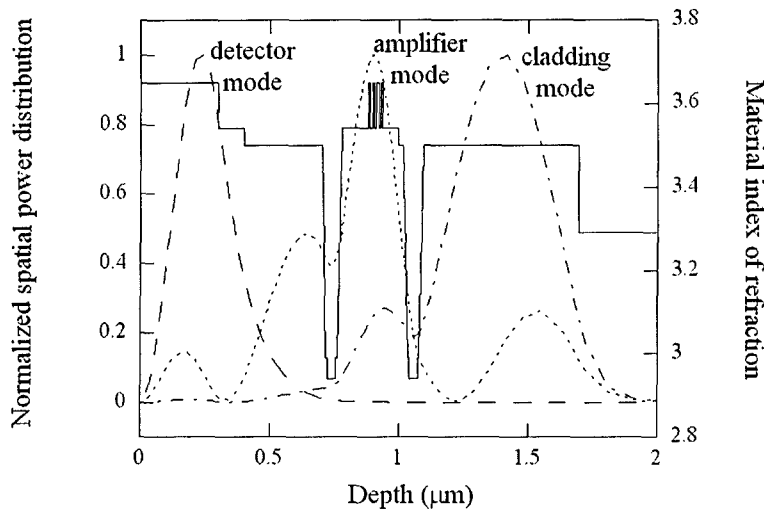
Figure 4.2. Refractive index profile and optical field, showing the detector mode, amplifier mode, and cladding mode.

and barely with the absorption region. These modes experience a relatively large net gain when amplifier modes are close to zero modal gain, producing a large increase in the guided optical power, but barely contributing to the total detected photocurrent. In order to fully understand the behavior of TAP detectors, we need to take into account the simultaneous presence of these three types of modes, together with the measurable photocurrent. We define the measurable photocurrent at a given gain diode bias current as the difference between the total detection diode current measured in the presence and in the absence of an optical input. As the input optical power increases, stimulated recombination depletes the carriers injected into the gain region at a faster rate, resulting in a lower production of spontaneous emission and ASE for the same gain diode bias current. This result in the measurable photocurrent being lower than the actual amount of photocurrent produced. This difference between actual and measurable photocurrent increases as the gain diode saturates and is a direct consequence of the impossibility to separate the detection diode current generated by absorption of either optical input signal, spontaneous emission, or ASE.

4.3 Spontaneous emission, ASE and background current

The importance of the different contributions to the background current in TAP detectors can be determined by the simultaneous measurement of the spontaneous emission and ASE produced in the device, together with the total background current. The InP-based devices had a p-i-n detector diode grown on top of the p-i-n amplifier diode. In this configuration, the stacking of p-n-p or n-p-n claddings, which allow current injection into the amplification active region and photocurrent extraction from the absorption active region, form a parasitic transistor. The middle cladding, between both active regions, plays the role of the base in the parasitic transistor, while the lower cladding below the gain region acts as emitter.
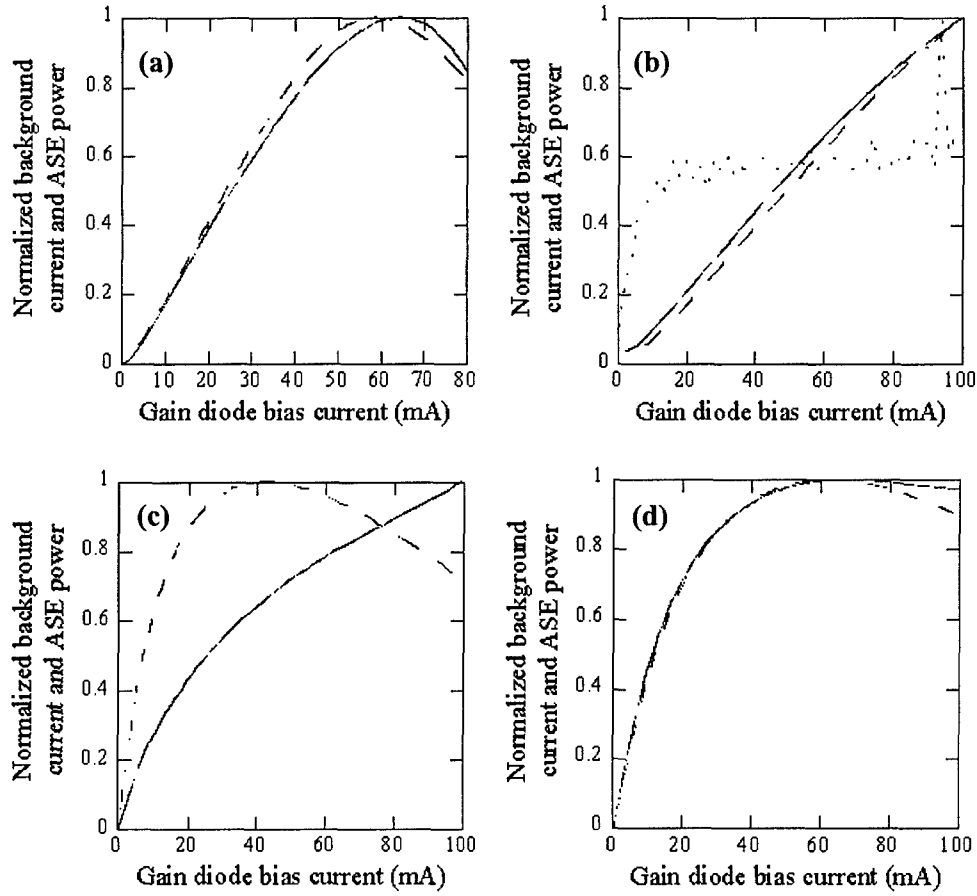
60

Figure 4.3. Simultaneous measurement of ASE generated in TAP detectors (dashed line) and total background current (solid line) as a function of the bias current in the gain diode. Results are shown for two GaAs-based TAP detectors with different design (Plot a and b), and from InP-based TAP detectors with n-p-n (c) and p-n-p (d) configurations.

Figure 4.3 shows the normalized measured ASE and background current for four different cases. Plots a and b compare measurements on GaAs devices with slightly different designs. Plots c and d show measurements performed on InP-based TAP detectors with n-p-n and p-n-p configurations, respectively. All devices were 200 μm long and had 3 μm wide active regions. The p-i-n absorption diode in the InP-based TAP detectors was reverse biased at 3 V. The absorption diode in the GaAs-based TAP detectors was a Schottky diode, which was unbiased. The main differences in the design between the two GaAs detectors (Plot a and b) were the number of QWs and the thickness of the n-doped cladding layer between the gain and absorption region. The initial design (Plot a) had 4 QWs and 300 nm of n-cladding. The improved design (Plot b) had 7 QWs and a 600 nm thick n-cladding. The purposes of these changes was to improve the guiding properties (reduce or eliminate cladding modes) and increase the amplifier gain. In both cases, the background current follows the ASE, suggesting that

61

the absorption of ASE is the main contribution to the background current. In Plot b, the non-guided, non-amplified spontaneous emission is also shown as a dotted line. A large amount of spontaneous emission naturally reaches the detector region, because of the geometry of these devices. However, it is interesting to note that the spontaneous emission curve flattens out relatively early, indicating that stimulated recombination (signal and ASE) dominates at higher drive currents. Absorption of non-amplified spontaneous emission is thus not a significant contributor to the background current. The earlier roll-of in the curves in Plot a indicates more heating in this design compared to Plot b. This is attributed to the smaller number of QWs in these devices, which naturally require higher drive current to reach the same gain level.

In the InP device with n-p-n configuration (Plot c), the background current increases monotonically and does not follow the roll-off in the ASE produced in the device, indicating a very significant contribution from the parasitic transistor. In the device with a p-n-p configuration (Plot d) however, the ASE and the background current evolve much more similarly, rolling-off nearly simultaneously. This indicates that the absorption of ASE generates most of the background current and that the transistor action is reduced. This is attributed to the shorter diffusion length of holes compared to electrons, which limits the current flow through the middle n-cladding in the p-n-p devices.

4.4 Experimental results, GaAs Based Devices

GaAs based TAP detectors were fabricated for operation around 850-nm wavelength. A schematic of the GaAs TAP detector is shown in Figure 4.4. The structure was grown by MBE on a semi-insulating GaAs substrate. The absorption region is a metal-semiconductor-metal (MSM) structure formed by a 200 nm GaAs layer sandwiched between the top metal contact and the n-doped contact layer with the common ground contact. Beneath this n-contact layer is the amplifier active region, which consisted of 7 GaAs QWs and AlGaAs barriers. On either side of the active region are AlGaAs layers with increased Al content to facilitate the creation of current and mode confinement
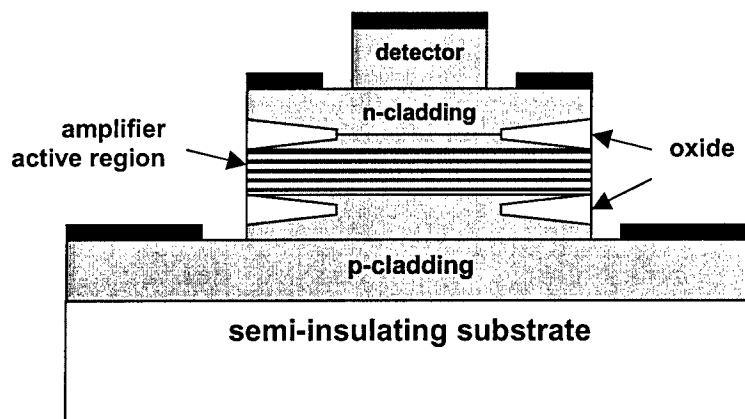

Figure 4.4. Schematic showing the design of the GaAs-based TAP detector

through wet thermal oxidation. On the bottom of the structure are p-doped contact and cladding layers. The oxidation layers provide numerous advantages. In addition to current and mode confinement, the high-Al content layers also produce a barrier for minority carriers, resulting in improved carrier confinement. This confinement improves the gain-current relation and, in addition, minimizes any transistor action by reducing the number of carriers injected into the "base."

The fabrication of GaAs based TAP detectors starts with the lift-off deposition of Ti/Pt/Au contacts to provide Schottky contact to the bulk intrinsic absorption region. Using this metal as a mask, the intrinsic region is etched, using a $H_2SO_4:H_2O_2:H_2O$ (1:4:40) solution. Next, Ni/AuGe/Ni/Au contacts to the intermediate n-cladding layer are deposited, and annealed at 420°C. The amplifier waveguide is etched using Cl_2 reactive ion etching (RIE). The contact to the p-doped bottom cladding is evaporated next, using Pd/Zn/Pd/Au, and subsequently annealed at 380°C. Wet oxidation at 400°C follows. The devices are then planarized using PMGI. Finally, thick Au interconnection CPW and gain pads are deposited, using Ti as a sticking layer. Figure 4.4 shows microscope pictures of completed devices. Note that the devices are staggered, so that with one cleave TAP detectors of different length are produced.
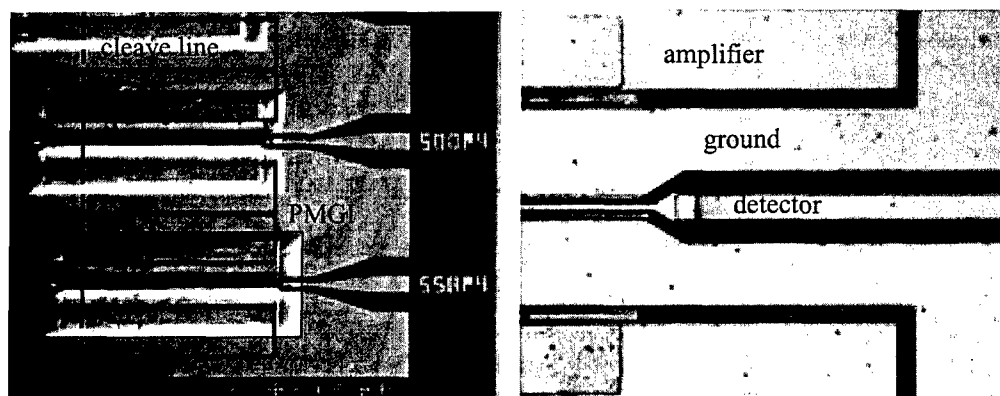

Figure 4.5. Photographs of fully processed GaAs TAP detectors.

As explained above, vertically coupled TAP detectors can support three different types of modes, each contributing differently to the photocurrent. Which modes dominate in the TAP detector depend not only on the waveguide design, but also on the coupling of light into the structure. In order to find the optimum position of the lensed fiber that launches the signal into the device, the photocurrent was measured versus amplifier bias current for different fiber positions. Figure 4.6 shows the measurable photocurrent in the GaAs TAP detectors as a function of the vertical displacement of the lensed fiber used to couple light into the device. 0 μm displacement correspond to the lowest position, from which most of the power coupled into the device feeds the cladding mode, and only a small fraction of it is transferred into the amplifier mode. As the displacement is increased (the fiber is moved upward), less optical power is coupled into the cladding mode, resulting in lower competition between signal and ASE for the available gain, with an ensuing increase in the measurable photocurrent. The measurable photocurrent finally decreases again as the fiber is moved above the point which produces optimum coupling into the amplifier mode. For positions above the amplifier

region (y = 3, 4 μm), the light is mostly coupled into the detector region, resulting in high photocurrent at low amplifier currents but only a moderate increase with increased amplifier current. For a vertical displacement of 2 μm (the dashed line), the increase in photocurrent with amplifier bias current is greatest, indicating optimum coupling into the amplifier mode and the most dramatic effect of the distributed absorption and amplification.
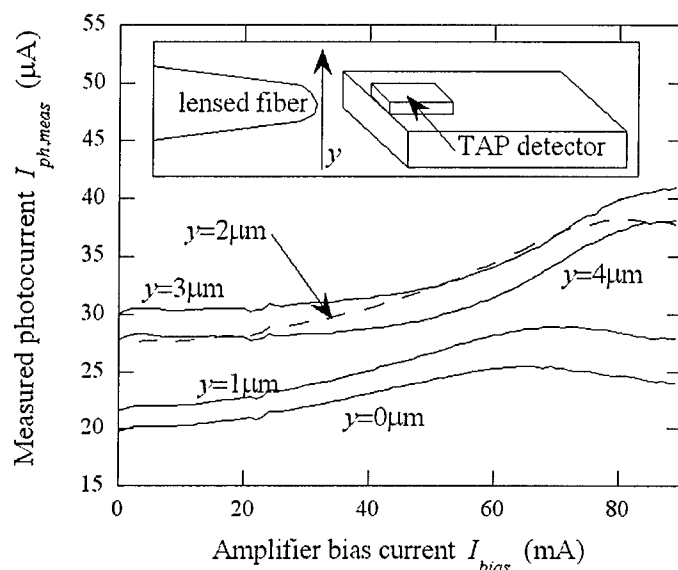

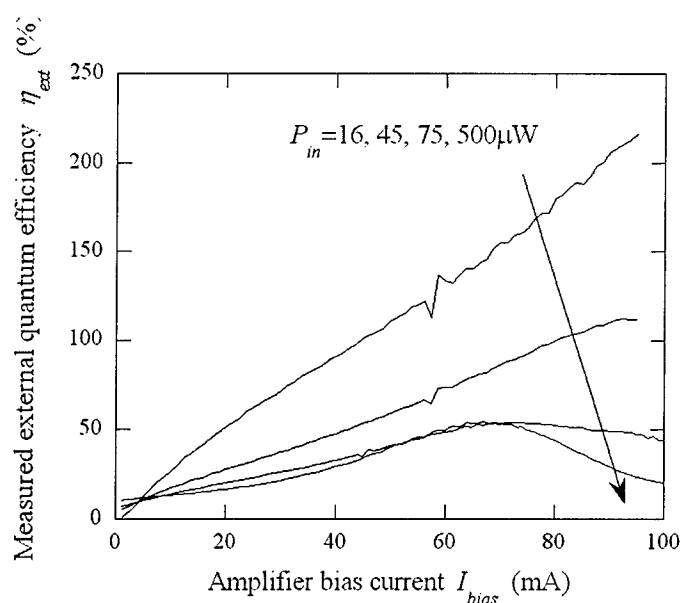*Figure 4.6. Photocurrent versus amplification for different fiber positions*

Figure 4.7. Measured external quantum efficiency in vertically coupled GaAs TAP detectors. More than 200 % efficiency is demonstrated.

64

Figure 4.7 shows measured external quantum efficiency vs. amplifier bias current for different input optical power. The device length was 200 μm and the input facet was not antireflection coated. Reduction in efficiency through competition between ASE and the optical signal is observed at higher optical signal powers. Over 200% differential efficiency is demonstrated for 16 μW input signal power.

4.5 Experimental results, InP Based Devices

InP based TAP detectors were fabricated for operation around 1.55μm wavelength. A schematic of the InP devices is shown in Figure 4.8. The devices combine a bulk InGaAs photodetector ridge region with a QW active region for amplification in a p-n-p structure. The structure was grown by MOCVD on a semi-insulating InP substrate. The absorber was 250 nm thick, and the amplifier active region had six compressively strained $In_{0.76}Ga_{0.24}As_{0.79}P_{0.21}$ quantum wells separated by strain-compensating $In_{0.71}Ga_{0.29}As_{0.55}P_{0.45}$ barriers. A thick n-InP cladding layer separated the absorption and gain region. The top p-contact was Ti/Pt/Au, the center n-contact consisted of Ni/AuGe/Ni/Au and finally a Pd/Zn/Pd/Au metallization was used for the bottom p-contact. After cleaving, the input facet of the TAP detectors was antireflection coated with 220 nm SiO_x. Figure 4.9 shows an SEM of a completed device.
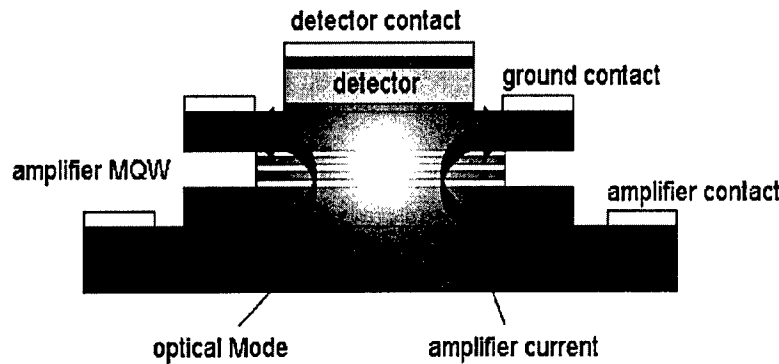

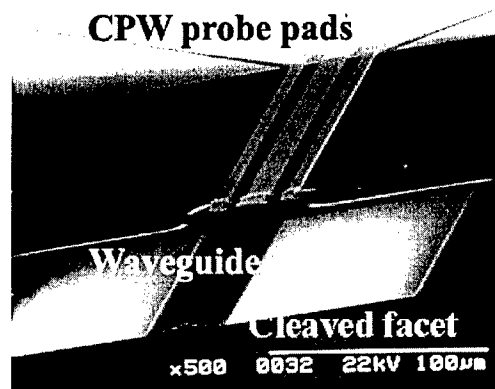
Figure 4.8. Schematic of InP-based TAP detector.

Figure 4.9. SEM of InP-based TAP detector.

Experimental results from InP-based TAP detectors are shown in Figure 4.10. Measurements were taken on a device that was 300 μm long and had a 3 μm wide absorption region. The external quantum efficiency is plotted vs. gain diode bias current. The input signal power was 2.1 μW. This device presents two main modes, one detector mode and one amplifier mode, each one of them overlapping marginally with the other active region. The low bias current efficiency may therefore be assigned almost exclusively to the detector mode, while the amplifier mode experiences large net gain as it propagates. This results in a rapidly increasing efficiency with the gain diode bias current for small optical powers (2.1 μW in figure 4.10), but also on saturation due to the large signal power when the input power increases (not shown in the figure). Over 100% external quantum efficiency is demonstrated.
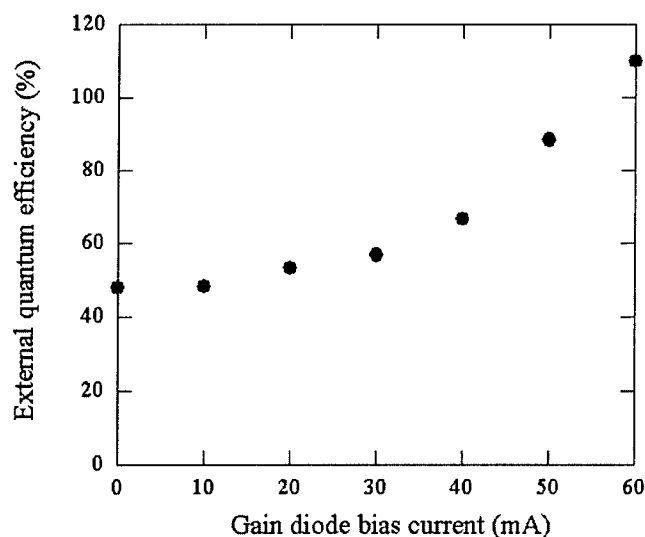
Figure 4.10. Measured external quantum efficiency in vertically coupled InP TAP detectors. More than 100 % efficiency is demonstrated.

4.6 Advantages of TAP Detectors with Alternating Gain and Absorption

The sequential TAP detector design (shown in Figure 4.1.a) present a number of advantages over the parallel configuration, as was outlined briefly above. Although the contribution to the total background current from absorption of spontaneous emission may be much smaller than the contribution from absorption of ASE in TAP detectors with vertical coupling, we believe this to happen only when amplifier modes experience relatively large net gain. In other words, at the most interesting operating point where the net modal gain approaches zero for amplifier modes, the contribution from spontaneous emission to the background current in TAP detectors with vertical coupling is far from negligible. A configuration featuring alternating gain and absorption significantly reduces this contribution to the background current. This reduction stems from the much smaller solid angle of absorption region subtended from any point in the amplification region, device length being in the order of a few hundreds of microns, while the width and thickness of the active regions are in the order of a few microns and a few hundred nanometers, respectively.

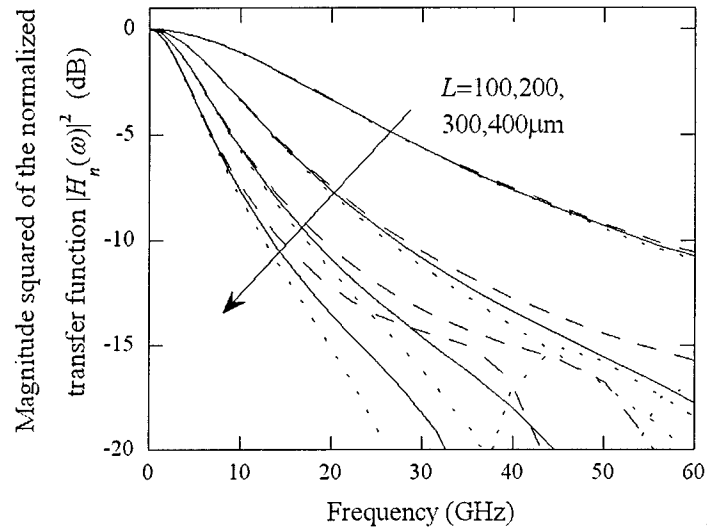*Figure 4.11. Simulated frequency response of TAP detectors with vertically coupled design. Δg is 0 (solid lines), -20 cm^{-1} (dashed lines), and 20 cm^{-1} (dotted lines).*
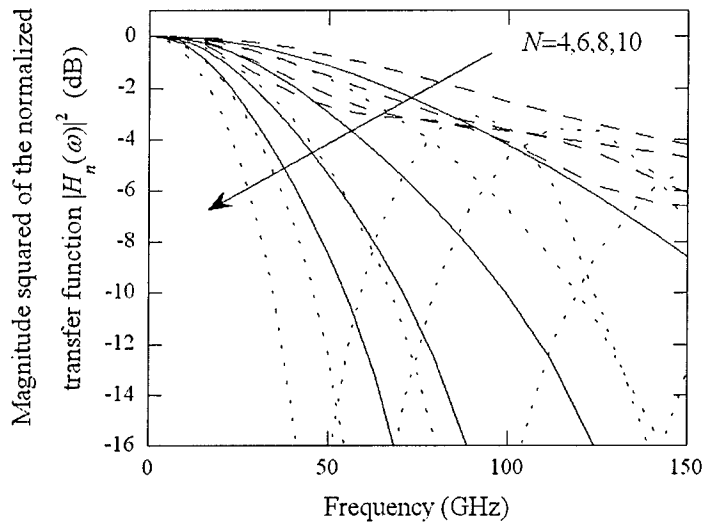

Figure 4.12. Simulated frequency response of TAP detectors with alternating gain and absorption regions. ΔG is 1 (solid lines), 0.5 (dashed lines), and 2 (dotted lines).
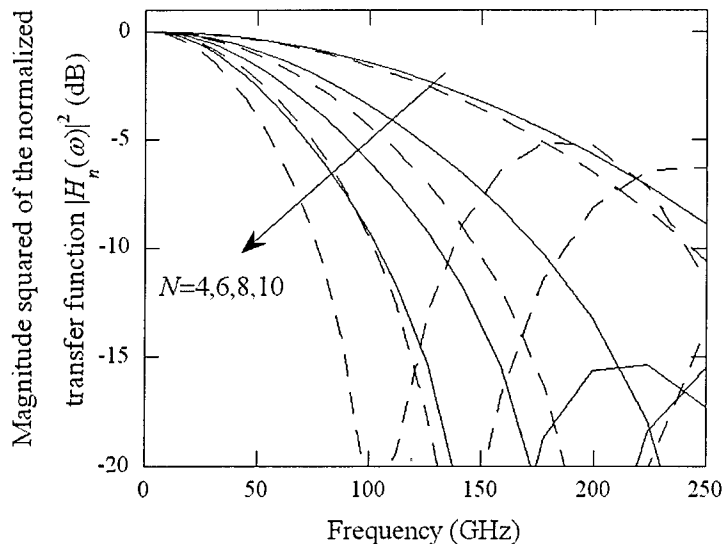
Figure 4.13. Simulated frequency response for TAP detectors with alternating gain and absorption regions, featuring 50-Ω termination at input and output. ΔG is 1 (solid lines), 0.5 (dashed lines), and 2 (dotted lines).

The superior microwave propagation performance is a direct consequence of the signal-carrying electrode being deposited mostly over insulator instead of doped semiconductor material. This electrode has a relatively small, periodic interaction with doped semiconductor layers, typically for about 10% of its total length. Distributed photocurrent simulations have shown this interaction to produce characteristic impedance close to 50 Ω, small velocity mismatch between electrical and optical velocities, and small microwave propagation loss. Figures 4.11 and 4.12 compare simulated high-speed performance for vertical and sequential TAP detectors, clearly demonstrating the advantage of the sequential design. The frequency response is plotted for different values of the net modal gain per unit length Δg and for different device lengths L in the case of the vertical design (Figure 4.11), and for different values of net gain per period ΔG and different number of periods N for the sequential design (Figure 4.11). All periods in the TAP detector with alternating gain and absorption are assumed to be identical, and their length is set at 50 μm. Figure 4.13 plots the simulated response of TAP detector with alternating gain and absorption presenting a 50-Ω terminated input where photocurrent contributions collected at both the input and output are added. This comparison allows us to determine the bandwidth-limiting factors in this configuration. It is noteworthy that two different features are shown in the frequency response: a slow roll-off (due to microwave propagation loss), and quasi-periodic dips generated by the addition of forward an backward propagating photocurrent contributions generated in each section. The improvement obtained with the 50-Ω terminated input is a clear consequence of the reduction in the phase delay of the backward traveling contribution, which is now collected at the input instead of being reflected and traveling all along the device to its output. The optimum device performance at this point occurs for a balanced contribution from all absorption sections, *i.e.*, when the power arriving to each detection section is the

same, whereas an imbalance towards a greater contribution close to the input (for net optical loss in each period) or close to the output (when each period provides net gain), results in a larger fraction of the photocurrent suffering destructive interference due to a larger relative phase delay caused by the path difference between forward- and backward-traveling contributions. We may therefore conclude that, due to the reduced, periodic interaction between the photocurrent-carrying electrode and doped semiconductor layers, TAP detectors with alternating gain and absorption do not suffer the effects of microwave propagation loss as severely as TAP detectors with vertical coupling, allowing for much larger device bandwidths. Note finally that, from the 3dB-bandwidth values extracted from Figures 4.11, 4.12, and 4.13, efficiency-bandwidth products in the order of 1THz are possible with external quantum efficiency values in the order of 10, which are indeed possible using this configuration.

In order to further improve the sequential design, optical filtering should be introduced between each section. This would reduce the amount of background current generated by spontaneous emission and ASE. Since the ASE generated in each gain section accumulates and gets amplified throughout all periods of the device, this would produce a very significant reduction in the total ASE contribution to the background current.

Publications

"Linearized modulator for monolithicallyintegrated photonic devices," L.A. Johansson, Y.A. Akulova, G.A. Fish and L.A. Coldren, *Proceeding Microwave Photonics*, Ogunquit, Maine, October 2004.

"Analog Performance of an InP Mach-Zehnder Modulator Integrated with a Widely Tunable Laser," L.A. Johansson, J.S. Barton, L.A. Coldren, *Proceedings Microwave Photonics*, Ogunquit, Maine, October 2004.

"Traveling-Wave Photodetectors With High Power-Bandwidth and Gain-Bandwidth Product Performance," D. Lasaosa, J.-W. Shi, D. Pasquariello, K.-G. Gan, M.-C. Tien, H.-H. Chang, S.-W. Chu, S.-K. Sun, Y.-J. Chiu, J. E. Bowers, *IEEE Journal of Selected Topics in Quantum Electronics,* vol. 10, no. 4, pp. 758-741, July/Aug. 2004.

"An Improved Approach of Optical Loss Measurement Using Photocurrent and Optical Transmission in an Electroabsorptiion Modulator," J. Shim, B. Liu, J. Piprek, and J. Bowers, *IEEE Photonics Technology Letters,* vol. 16, no. 6, pp. 1474-1476, June 2004.

"Nonlinear Properties of Traveling-Wave Electroabsorption Modulator," J. Shim, B. Liu, J. Piprek, and J.E. Bowers, *IEEE Photonics Technology Letters,* vol.16, no.2, pp. 1035-1037, April 2004.

"High-Speed Optical Frequency Modulation in a Monolithically Integrated Widely-Tunable Laser - Phase Modulator," L.A. Johansson, J.S. Barton, L.A. Coldren, G.A. Fish, *Optical Fiber Communication Conference (OFC2004),* March 2004.

"Demonstration of Widely-Tunable Single-Chip 10 Gb/s Laser-Modulators Using Multiple-Bandgap InGaAsP Quantum-Well Intermixing," J.W. Raring, E.J. Skogen, L.A. Johansson, M. Sysak, J.S. Barton, M.L. Masanovic, and L.A. Coldren, *IEEE Photonics Technology Letters,* 2004.

"Slope Efficiency and Dynamic Range of Traveling-Wave Multiple-Quantum-Well Electroabsorption Modulators," B. Liu, J. Shim, Y-J. Chiu, H.-F. Chou, J. Piprek, J. E. Bowers, *IEEE Photonics Technology Letters,* vol.16, no.2, pp. 590-592, Feb.2004.

"Sampled-grating DBR laser integrated with SOA and tandem electroabsorption modulator for chirp-control," L.A. Johansson, Y.A. Akulova, G.A. Fish and L.A. Coldren, *Electronics Letters,* vol. 40, pp. 70-71, Jan. 2004.

"Sampled-grating DBR laser-based analog optical transmitters", L.A. Johansson, J.T. Getty, Y.A. Akulova, G.A. Fish, L.A. Coldren, *Journal of Lightwave Technology,* vol. 21, pp. 2968-2976, Dec. 2003.

"Analog Characterization of Low-Voltage MQW Traveling-Wave Electroabsorption Modulators,' B. Liu, J. Shim, Y.-J. Chiu, A. Keating, J. Piprek, and J. E. Bowers, *Journal of Lightwave Technology Letters,* vol. 21, no. 12, pp. 3011- 3019, December 2003.

"CW Operation of 1.55 μm Bipolar Cascade Laser with Record Differential Efficiency, Low Threshold, and 50Ω Matching," J.T. Getty, E.J. Skogen, L.A Johansson, L.A. Coldren, *IEEE Photonic Technology Letters,* vol. 15, no. 11, pp. 1513-1515, November 2003.

"Postgrowth control of the quantum-well band edge for the monolithic integration of widely tunable lasers and electroabsorption modulators," E.J Skogen, J.W. Raring, J.S. Barton, S.P. DenBaars, L.A. Coldren, *IEEE Journal of Selected Topics in Quantum Electronics,* vol. 9, no. 5, pp. 1183-1190, Sept.-Oct. 2003.

"Chirp-Controlled Tandem Electroabsorption Modulator Integrated with an SOA and a Sampled-Grating DBR Laser," L.A. Johansson, Y.A. Akulova, G.A. Fish, L.A. Coldren, *Proc. LEOS 2003,* vol. 1, pp. 433-434, Tucson, Arizona, October 2003.

"1.55-mm bipolar cascade segmented ridge lasers," J.T. Getty, L.A. Johansson, E.J. Skogen and L.A. Coldren, *IEEE Journal of Selected Topics in Quantum Electronics,* vol. 9, pp. 1138-1145, Sept./Oct. 2003.

"Wavelength Agile, Integrated Optical Transmitters for Analog Applications," L.A. Johansson, Y.A. Akulova, G.A. Fish, L.A. Coldren, *Proc. SPIE,* vol. 5248, pp. 95-102, Orlando, Florida, September 2003.

"High-Speed Direct Modulation of 50Ω Bipolar Cascade Segmented Lasers," J.T. Getty, L.A. Johansson, E.J. Skogen, L.A. Coldren, *Proc. ECOC-IOOC,* paper no. We4.P.91, pp. 738-739, Rimini, Italy, September 21-25, 2003.

"Photocurrent Effects in an Electroabsorption Modulator Integrated with SGDBR Laser," L.A. Johansson, Y.A. Akulova, G.A. Fish, and Larry A. Coldren, *Proceedings Microwave Photonics,* pp. 161-164, Budapest, Hungary, September 2003.

"Widely-Tunable EAM-Integrated SGDBR Laser Transmitter for Analog Applications," L.A. Johansson, Y.A. Akulova, G.A. Fish, and L.A. Coldren, *IEEE Photonics Technology Letters,* vol. 15, no. 9, pp. 1285-1287, September 2003.

"InP-based waveguide photodetector with integrated photon multiplication," D. Pasquariello, J. Piprek, D. Lasaosa, J. E. Bowers, *SPIE Proceedings 5248-34, Semiconductor Optoelectronic Devices for Lightwave Communication, ITCOM'03,* Sept. 2003.

"Recent Advances in Photodetectors with Distributed Optical Amplification," D. Lasaosa, D. Pasquariello, J. Piprek, and J. E. Bowers, *SPIE Proceedings 5246-87, Active and Passive Optical Components for WDM Communications III, ITCOM'03,* Sept. 2003.

"Traveling-Wave Photodetector with Integrated Light Amplification," J. Piprek, D. Lasaosa, D. Pasquariello, J. E. Bowers, *Technical Digest of Conference on Lasers and Electro-Optics (CLEO'03)*, June 2003, Baltimore, MD.

"Novel Waveguide Photodetectors on InP with Integrated Light Amplification," J. Piprek, D. Pasquariello, D. Lasaosa, J. E. Bowers, *Compound Semiconductors, ECS Proceedings 2003-04*, pp. 1-8, 2003.

"Optimization of GaAs Amplification Photodetectors for 700% Quantum Efficiency," J. Piprek, D. Lasaosa, D. Pasquariello, J. E. Bowers, *IEEE Journal of Selected Topics in Quantum Electronics, Issue on Optoelectronic Device Simulation,* Vol. 9, No. 3, pp. 776-782, May-June 2003.

"1.55 µm Traveling-Wave Amplification Photodetector," J. Piprek, D. Pasquariello, D. Lasaosa, Y. Okuno, J. E. Bowers, *Proceedings of the 15th Conference on Indium Phosphide and related Materials (IPRM'03),* May 2003, Santa Barbara, CA.

"Segmented 1.55 µm laser with 400% differential quantum efficiency", J. Getty, E. Skogen, L. Coldren, *Optical Fiber Communications Conference, OFC 2003*, pp.183-184 vol. 1, 23-28 March 2003.

"Standing-Wave Enhanced Electroabsorption Modulator for 40-GHz Optical Pulse Generation," Hsu-Feng Chou, Yi-Jen Chiu, and John E. Bowers, *IEEE Photonics Technology Letters*, vol.15, no.2, pp. 215-217, Feb. 2003.

"High Optical Power Electroabsorption Waveguide Modulator," L.A. Johansson, Y.A. Akulova, G.A. Fish and L.A. Coldren, *Electron. Lett.,* vol. 39, no. 4, pp. 364-365, February 2003.

"Physics of Waveguide Photodetectors with Integrated Amplification," J. Piprek, D. Lasaosa, D. Pasquariello, J. E. Bowers, *SPIE Proceedings 4986-28, Physics and Simulation of Optoelectronics Devices XI, Photonics West,* Jan. 2003.

"High Extinction Ratio And Saturation Power Traveling-Wave Electroabsorption Modulator," Y.-J. Chiu, H.-F. Chou, V. Kaman, P. Abraham, J.E. Bowers, *IEEE Photonics Technology Letters,* vol. 14, no. 6, pp. 792-794, June 2002.

"Using Standing-wave Electroabsorption Modulators to Generate 40GHz Optical Pulses," H.-F. Chou, Y.-J. Chiu J. E. Bowers, *Conference on Laser and Electro-Optics (CLEO'2002), paper CMI1*, pp. 41-42, June 2002, Long Beach, CA.

"High-Efficiency Multi-Quantum-Well Electroabsorption Modulators," J. Piprek, Y.-J. Chiu, S. Zhang, J. E. Bowers, C. Prott, H. Hillmer, *Proceedings of the ECS Symposium on Integrated Optoelectronics*, May 2002, Philadelphia, PA.

"40GHz Optical Pulse Generation Using Sinusoidally-Driven Traveling-Wave Electroabsorption Modulator," H.-F. Chou, Y.-J. Chiu, J.E. Bowers, *Electronics Letters,* vol. 38, no. 8, pp. 379-380, April 2002.

"Widely tunable directly modulated sampled-grating DBR lasers," M.L. Majewski, J. Barton, L.A. Coldren, Y. Akulova, M.C. Larson, *Optical Fiber Communication Conference (OFC 2002),* pp. 537-538, 17-22 March 2002.

"High-performance EAM-integrated SGDBR laser for WDM microwave photonic applications," L.A. Johansson, J.S. Barton and L.A. Coldren, *International Topical Meeting on Microwave Photonics,* 2002, pp. 61 – 64, 5-8 Nov. 2002.

"Noise and distortion properties of widely-tunable sampled-grating DBR lasers," H.X. Shi, D.A. Cohen, J. Barton, M. Majewski, L.A. Coldren, M.C. Larson, G.A. Fish, *LEOS 15th Annual Meeting (LEOS'02),* vol. 2, pp. 801-802, Nov. 2002.

"A quantum-well-intermixing process for wavelength-agile photonic integrated circuits," E. J. Skogen, J.S. Barton, S.P. Denbaars, L.A. Coldren, *IEEE Journal of Selected Topics in Quantum Electronics,* vol. 8 , no. 4, pp. 863-869, July-Aug. 2002.

"40GHz Optical Pulse Generation Using Traveling-Wave Electroabsorption Modulator," H.-F. Chou, Y.-J. Chiu, J. E. Bowers, *Technical Digest of 27th Optical Fiber Communication Conference (OFC'02),* paper WV2, pp. 338-339, March 2002, Anaheim, CA.

"Widely tunable electroabsorption-modulated sampled-grating DBR laser transmitter", Y.A. Akulova, G.A. Fish, Ping-Chiek Koh, C.L. Schow, P. Kozodoy, A. P. Dahl, S. Nakagawa, M.C. Larson, M.P. Mack, T.A. Strand, C.W. Coldren, E. Hegblom, S.K. Penniman, T. Wipiejewski, L.A. Coldren, *IEEE Journal of Selected Topics in Quantum Electronics,* vol. 8, pp. 1349 –1357, 2002.

"Dynamic range of widely tunable sampled grating DBR lasers," H.X Shi, D. Cohen, J. Barton, M. Majewski, L.A. Coldren, M.C. Larson, G.A. Fish, *Electronics Letters,* vol. 38, no. 4, pp. 180-181, 14 Feb. 2002.

"Relative intensity noise measurements of a widely tunable sampled-grating DBR laser," Shi Hanxing, D. Cohen, J. Barton, M. Majewski, L.A. Coldren, M.C. Larson, G.A. Fish, *IEEE Photonics Technology Letters,* Vol. 14, No. 6, pp. 759-761, June 2002.

"Direct intensity modulation in sampled-grating DBR lasers," M.L. Majewski, J. Barton, L.A Coldren, Y. Akulova, M.C Larson, *IEEE Photonics Technology Letters,* vol. 14, no. 6, pp. 747-749, June 2002.

"Analysis of Multi-Quantum Well Electroabsorption Modulators," J. Piprek, Yi-Jen Chiu, J. E. Bowers, *SPIE Proceedings 4646-77, Physics and Simulation of Optoelectronic Devices X, Photonics West,* January 2002, San Jose, CA.

"Low-voltage traveling-wave electroabsorption modulator," Yi-Jen Chiu, V. Kaman, S.Z. Zhang, J. Piprek, J.E. Bowers, *Conference Proceedings of IEEE/ LEOS 14th Annual Meeting (LEOS 2001),* vol. 1, pp. 182-183, Nov. 2001, San Diego, CA.

"Distributed effects model for cascaded traveling-wave electroabsorption modulator," Yi-Jen Chiu, V. Kaman, S.Z. Zhang, J.E. Bowers, *IEEE Photonics Technology Letters,* vol. 13, no. 8, pp. 791-793, Aug. 2001.

"High-Speed Traveling-Wave Electroabsorption Modulators," Yi-Jen Chiu, Sheng Z. Zhang, Volkan Kaman, Joachim Piprek, John E. Bowers, *Symposium on Radio Frequency Photonic Devices and Systems II, 46th SPIE Annual Meeting,* Aug. 2001, San Diego, CA.

"Modeling of traveling-wave amplification photodetectors," Daniel Lasaosa, Yi-Jen Chiu, Joachim Piprek, John E. Bowers, *SPIE Proceedings 4283-64, Physics and Simulation of Optoelectronic Devices IX, Photonics,* Jan. 2001, San Jose, CA.

"Noise Model for Photodetectors With Distributed Optical Amplification and Absorption," Daniel Lasaosa, David D'Alessandro, Guido Giuliani, Yi-Jen Chiu, Joachim Piprek, John E. Bowers, *International Workshop on Numerical Simulation of Optoelectronic Devices,* 2001, Santa Barbara, CA.

"Traveling-wave Amplification Photodetector (TAP detector)," Daniel Lasaosa, Yi-Jen Chiu, Joachim Piprek, John E. Bowers, *Conference Proceedings of IEEE/LEOS 13th Annual Meeting (LEOS 2000),* Nov. 2000, Rio Grande, Puerto Rico.

"Low-Bias and High-Saturation Power Traveling-Wave Electroabsorption Modulator by Using InGaAsP/InGaAs MQW," Y.-J. Chiu, V. Kaman, P. Abraham, S. Z. Zhang, J. E. Bowers, *Conference Proceedings of IEEE/LEOS 13th Annual Meeting (LEOS 2000),* Nov. 2000, Rio Grande, Puerto Rico.

"High-Speed Operation of Travelling-Wave-Electro-Absorption Modulator," V. Kaman, S.Z. Zhang, A.J. Keating, J.E. Bowers, *Electronics Letters,* vol. 35, no. 12, pp. 993-995, June 1999.

"25-GHz Polarization-Insensitive Electroabsorption Modulators with Traveling-Wave Electrodes," Sheng Z. Zhang, Yi-Jen Chiu, Patrick Abraham, John E. Bowers, *IEEE Photonics Technology Letters,* vol. 11, no. 2, pp. 191-193, Feb. 1999.